AEROELASTIC DESIGN OF A LIGHTWEIGHT DISTRIBUTED ELECTRIC PROPULSION AIRCRAFT WITH FLUTTER AND STRENGTH REQUIREMENTS

A Thesis
Presented to
The Academic Faculty

by

Sui An

In Partial Fulfillment
of the Requirement of Degree
Master of Science in the
School of Aerospace Engineering

Georgia Institute of Technology
May 2015

AEROELASTIC DESIGN OF A LIGHTWEIGHT DISTRIBUTED ELECTRIC PROPULSION AIRCRAFT WITH FLUTTER AND STRENGTH REQUIREMENTS

Approved by:

Dr. Graeme J. Kennedy
School of Aerospace Engineering
Georgia Institute of Technology

Dr. Dewey H. Hodges
School of Aerospace Engineering
Georgia Institute of Technology

Dr. Brian J. German
School of Aerospace Engineering
Georgia Institute of Technology

Date Approved: April, 20, 2015

ACKNOWLEDGEMENTS

This research paper is made possible through the help and support from everyone, including: Teachers, family, friends. Especially, please allow me to dedicate my acknowledgment of gratitude toward the following significant advisors and contributors:

First and foremost, I would like to thank Dr. Graeme J. Kennedy for his most support and encouragement. He gave me advise on researching on the whole period. He also kindly read my paper and offered invaluable detailed advice on grammar, organization.

Second, I would like to thank Dr. Dewey H. Hodges and Dr. Brian J. German to read my thesis and to provide valuable advice.

I sincerely thank to my parents, family, and friends, who provide the advice and financial support. Thank you for providing me comfort when I feel low. The product of this research paper would not be possible without all of them.

Finally, I want to address special gratitude to Mr. Jiang Fengze for driving me home every night no matter how late I stayed at lab in the last month.

TABLE OF CONTENTS

LIST OF TABLES

LIST OF FIGURES

SUMMARY

Distributed electric propulsion is a promising technology currently being considered for general aviation-class aircraft that has the potential to increase range and performance without sacrificing low-speed flight characteristics. However, the high-aspect ratio wings enabled by distributed electric propulsion make these designs more susceptible to adverse aeroelastic phenomena. This thesis describes the development of a gradient-based optimization framework for aircraft with distributed electric propulsion using structural and aeroelastic constraints. The governing equations for the coupled aeroelastic system form the basis of the static aeroelastic and flutter analysis. In this work, the Doublet-Lattice method is used to evaluate the aerodynamic forces exerted on the wing surface. In order to consider the impact of propeller-induced flow on aerodynamic loading, a one-way propeller-wing coupling is computed by superposition of the propeller induced velocity profile calculated using actuator disk theory and the wing flow field. The structural finite-element analysis is performed using the Toolkit for the Analysis of Composite Structures (TACS). The infinite-plate spline method is used to perform load and displacement transfer between the aerodynamic surface and the structural model. Instead of utilizing a conventional flutter analysis, the Jacobi-Davidson method is used to solve the governing eigenvalue problem without a reduction to the lowest structural modes, facilitating the evaluation of the gradient for design optimization. This framework is applied to different configurations with distributed electric propulsion to mini-

mize structural weight subject to structural and aeroelastic constraints. The effect of flutter constraints, wing aspect ratio, and electric propeller quantity are compared through a series of design optimization studies. The results show that larger aspect ratio wings and more electric motors lead to heavier wings that are more susceptible to flutter. This framework can be used to develop lighter aircraft with distributed electric propulsion configuration that satisfy strength and flutter requirements.

CHAPTER 1

INTRODUCTION

Distributed electric propulsion (DEP) aircraft use electric motors distributed about the vehicle to provide thrust for propulsion. DEP is a promising technology that has the potential to be integrated into a wide number of future civil and general aviation transport aircraft [Gohardani et al., 2011]. DEP has the potential to improve performance in noise reduction, aerodynamic efficiency and flight safety. However, the benefits of these innovative configurations also brings new aeroelastic challenges. In particular, DEP configurations may be more susceptible to adverse aeroelastic phenomena due to the high aspect-ratio wings and distributed mass of the mounted electric motors. Therefore, including the impact of aeroelastic phenomena is an important aspect of the design process.

An assessment of the impact of aeroelasticity on the DEP configuration has not been adequately examined in literature. In this research, a gradient-based optimization framework for DEP aircraft design with strength and flutter constraints was developed. In this research, gradient-based optimization method is applied to obtain a detailed structural design. The gradient-based optimization method enables the exploration of a larger design space compared with gradient-free optimization schemes. This framework can be used to optimize DEP aircraft wings to achieve minimum weight while satisfying both aeroelastic constraints and the stress constraints.

In formulating the flutter constraint, it is important to estimate aerodynamic loads exerted on the wing surface. In this research, the Doublet-Lattice method (DLM) is used to conduct aerodynamic analysis and estimate the load on the wing. The coupling between the propeller induced velocity profile and wing surface affects DEP aircraft performance significantly since it changes the local upwash velocity used by the DLM to compute the pressure difference. This pressure difference is the main reason for DEP aircraft high aerodynamic efficiency. This interaction will be considered by superposition of an isolated propeller induced velocity field with the upwash velocity field calculated by the DLM. The propeller

induced flow profile is computed using the actuator theory.

Most previous approaches conduct flutter analysis by reducing the structural response to the lowest natural modes. This modal reduction can be costly to compute and cannot be easily differentiated in a computationally efficient manner. To overcome these disadvantages, a flutter analysis technique was developed for aeroelastic models that do not perform modal reduction and are compatible with large-scale finite-element structural models. This approach uses the Jacobi-Davidson method to determine the lowest modes of the full aeroelastic system. In this way, the derivatives can be computed without this modal reduction, which is simpler and faster.

The stress constraints are evaluated using a coupled static aeroelastic code developed for gradient-based optimization. This coupled code performs the aerodynamic analysis using Tripan, which is a three-dimensional panel method for the solution of the Prandtl-Glauert equation, and the structural finite-element analysis using the Toolkit for the Analysis of Composite Structures (TACS). The Tripan is used as an aerodynamic solver; its aim is to estimate the aerodynamic loading. TACS is used as a structural solver which couples the aerodynamic loading from Tripan and obtains the displacement and stresses in the structure.

Finally, the gradient-based optimizer HOpt is used to solve the flutter-constrained optimization problem. HOpt is a python-based optimizer for parallel large-scale gradient-based optimization which uses an interior-point method. With all of the techniques and components introduced above, the optimization framework is complete and ready to generate the optimized structure design result. In the result, three categories of outcomes are obtained. First, a stress-constrained minimum mass designs without a flutter constraint is obtained. Next, the effect of the flutter constraint is evaluated by obtaining results that include the proposed flutter constraint. Finally, the impact of the aspect ratio and propeller quantity is studied through a parameter study.

This thesis is organized as follows. In the first chapter, a general introduction is provided. In the chapter two, aeroelasticity and the distributed electric propulsion concept is reviewed. The aeroelasticity section includes static aeroelasticity and an introduction to flutter. In the distributed electric propulsion concept part, the advantage and development potential of distributed propulsion configurations is shown, followed by introduction of prototypes with this configuration. In the third chapter, the theory applied in the research is briefly introduced. This includes the theory used to set up the optimization problem, define functions of interest, derive the coupled governing equations of the system, and the general procedure of the design optimization. In the fourth chapter, detailed information about the procedures and

techniques of the optimization process is introduced, including the Doublet-Lattice method, propeller actuator disk theory, one way propeller-wing coupling for the aerodynamic analysis, and the Jacobi-Davidson method used to solve the large-scale flutter eigenproblem. This includes the Infinite Plane Spline (IPS) for load and displacement transfer, TACS, which is used for finite-element analysis and TriPan which is used for aerodynamic analysis. The optimizer, the HOpt is also introduced in this chapter. In the fifth chapter, optimization result and analysis is presented. The sixth chapter describes future work which can improve the optimization framework.

CHAPTER 2

BACKGROUND

2.1 Aeroelasticity concept

Aeroelasticity is the study of the mutual interaction between aerodynamic forces, elastic forces, inertial force, and the influence of this interaction on aircraft design [Bisplinghoff et al., 1996]. Depending on whether inertial forces are considered, aeroelastic phenomenon can be divided into two categories: static aeroelasticity which is also called aerostructural analysis, and dynamic aeroelasticity. By definition, static aeroelasticity is not time-dependent, and inertial forces are eliminated from the equilibrium equations.

Flutter, buffeting, and gust response are common dynamic aeroelastic phenomena that must be considered in the aircraft design process. Flutter is a dynamic instability of an elastic body in an airstream [Bisplinghoff et al., 1996]. Methods of predicting flutter for linear structural model include the $p-$method, the $k-$method, and the $p-k$ method [Hodges and Pierce, 2011]. For nonlinear systems, flutter manifest itself as a limit cycle oscillation (LCO), and methods from the study of dynamic systems can be used to determine the speed at which flutter will occur, which is called the critical flutter speed [Tang and Dowell, 2004]. Flutter can also occur on structures other than aircraft. One famous example of flutter phenomena is the collapse of the original Tacoma Narrows Bridge [Billah and Scanlan, 1991].

Aeroelastic phenomenon plays a critical role in the design of many aerospace vehicles including civil airliners and rockets with slender bodies. Some of the typical aeroelastic problems, such as static aeroelastic divergence, flutter and elastic load correction keep occurring in the aircraft design process. In modern aircraft design, aeroelasticity design and optimization becomes more and more important since pursuing lighter structure weight and higher performance at the same time is a widely noticed trend. Reducing structure weight will possible deteriorate structure strength as well as stiffness. While higher performance is always followed by larger loads exerting on the structure. So guaranteeing aircraft structure

while satisfying aeroelasticity constraint is critical in the design process.

2.2 Distributed electric propulsion concept

Figure 2.1: NASA Leading Edge Asynchronous Propellers Technology (LEAPTech) DEP concept[1]

Distributed electric propulsion (DEP) is typically accomplished by spanwise distribution of multiple electric motors with propellers across the wing as seen in Figure 1. The goal of the proposed concept is to increase performance in noise reduction, aerodynamic efficiency and flight safety, as compared to the conservative configuration use of a smaller number of large engines, jets or propellers. By utilizing multiple electric motors to meet thrust requirements, all the propellers spin at relatively low speeds which can minimize noise during flight [Alex et al., 2014]. The electric motors mounted along the wing leading edge can increase dynamic pressure over the wing, especially during the take-off and landing period resulting in better take-off and landing performance [Alex et al., 2014]. Another advantage of DEP is improving safety by motor redundancy. With multiple motors, a single engine malfunction condition is not a critical situation to the aircraft performance and much of available thrust and controllability will not be lost. The distributed concept also has better gust load alleviation ability. The load redistribution provided by the engines has the potential to alleviate gust load problems, while providing passive load alleviation resulting in a lower wing weight [Leifsson et al., 2013].

[1] [Patterson and German, 2014]

Numerous authors have conducted research projects in distributed electric propulsion aircraft. NASA's research efforts in collaboration with a number of partner universities and research institutes has successfully contributed to aspects of distributed propulsion technology [Kim and Saunders, 2003, Ko et al., 2003]. Cranfield University has also taken steps towards the exploration of distributed concept [Ameyugo et al., 2006]. Patterson and German developed tools to estimate the aerodynamic forces considering the coupling between distributed propellers and wings [Patterson and German, 2014, Patterson et al., 2013]. Gohardani has a detailed research review in this field [Gohardani et al., 2011].

Figure 2.2: The Helios Prototype flying wing in flight. Credit:NASA.org

Many distributed propulsion aircraft prototypes have been developed. The NASA Helios in Figure 2.2 has 14 electric motors with propellers mounted at the wing leading edge, powered by solar and fuel cell system. Helios was the fourth and last prototype in a series of unmanned aerial vehicles (UAV). Under NASA's Environmental Research Aircraft and Sensor Technology (ERAST) program,the AeroVironment Inc. developed and test flew this aircraft in 1999. The goal of this program was to develop high-altitude aircraft that can perform atmospheric research and serve as communication platforms.

Unfortunately, this prototype crashed on June, 26th, 2003, during a long endurance mission. Large wing deflection and oscillation were the main reasons for this catastrophe. The aircraft encountered turbulence thirty minutes into the flight and suffered from a high wing dihedral deflection. This resulted in severe oscillation and deviation which led to the

solar cell and skin departure from the aircraft.

More recently, the University of Michigan designed and manufactured a UAV with a very flexible wing structure and DEP configuration. Seen in Figure 2.3, the name of this UAV is X-HALE, . It has an 8 m span, with a wing constructed with eight identical 1 m sections. The chord length is 0.2 m. The aircraft also has four 0.83 m booms with horizontal tails attached. X-HALE has a mass of 11 kg. The anticipated flight speed ranges from 10 to 19 m/s. This innovative aircraft is used as a test flight platform in area such as nonlinear control and flexible wing aeroelasticity [Cesnik and Su, 2011, Cesnik et al., 2010].

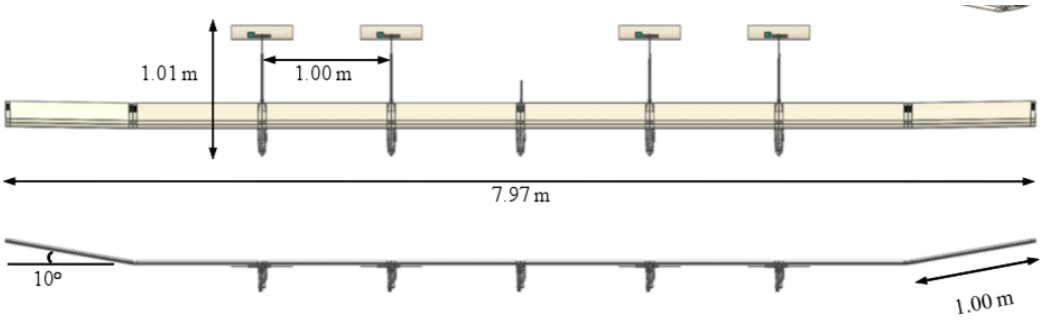

Figure 2.3: Complete X-HALE CAD assembly: top, and front views[1]

The Leading Edge Asynchronous Propellers Technology (LEAPTech) in Figure 2.4 is one the recently promising DEP aircraft programs and is conduct by Joby Aviation in cooperation with NASA and ESAero. The LeapTech program's aim is to bring significant aerodynamic improvements in efficiency which can reduce as mush as 60% drag, and also improve ride quality and gust sensitivity by doubling the wing loading. With their efforts, the max lift coefficient can reach as high as 5. Other performance parameters, such as field length and stall speed, maintain the same as conventional aircraft powered by gas. Furthermore, the noise signature is reduced by using electric motors and slow-speed propellers. More detailed technical specifications [Alex et al., 2014] are shown in the Table 2.1.

[1] [Cesnik and Su, 2011]

Table 2.1: Technical specifications of the LEAPTech aircraft

Parameter	Value
Seating capacity	4
Gross weight	1350 kg
Wing area	5.1 m^2
Wingspan	9.4 m
Aspect ratio	17.4
Wing loading	266 kg/m^2
Cruise speed	320 km/h
Cruise altitude	3650 m

Figure 2.4: A rendering of the LEAPTech aircraft. Credit: Joby Aviation

Recently, the LEAPTech aircraft wing component conducted a truck test at NASA Armstrong research center, as seen Figure 2.5. This truck experiment is a precursor for further developments of a small prototype aircraft equipped with DEP wing. Researchers at the Joby aviation plan to substitute the wing of a Tecnam P2006T general aircraft with a DEP system which will allow researchers to compare performance improvement easily [Alex et al., 2014].

All of these DEP prototypes share some characteristics. They all have high aspect ratio wing so the structure is very flexible, and can have large deflections in flight under aerodynamic loading. This causes aeroelasticity and component stress that can be a serious and

Figure 2.5: The LEAPTech aircraft wing under truck test. Credit: Joby Aviation

critical constraint during flight. As a result, conducting aeroelasticity optimization as well as strength constraint is essential to aircraft safety.

CHAPTER 3

PROBLEM STATEMENT AND METHODOLOGY

3.1 Problem setup

The purpose of this research is to develop a gradient-based optimization framework to conduct design optimization of flexible, lightweight aircraft with a DEP configuration. The research will focus on investigating how to achieve optimal aircraft structural design while satisfying all the imposed constraint. Also the effect of the DEP configuration changing the strength and aeroelastic characteristics of a lightweight conventional wing structure with a large aspect ratio will be investigated.

This approach can be described as an optimization problem in which the goal is to minimize an objective function while satisfying all the aeroelastic and structural constraints. The optimization problem can be expressed as

$$\begin{aligned} &\underset{x}{\text{minimize}} && f(\boldsymbol{x}, \boldsymbol{u}) \\ &\text{with respect to} && \boldsymbol{x}, \boldsymbol{u} \\ &\text{governed by} && \boldsymbol{R}(\boldsymbol{x}, \boldsymbol{u}) = 0 \\ &\text{such that} && \boldsymbol{F}_i(\boldsymbol{x}, \boldsymbol{u}) \leq 1 \\ & && \boldsymbol{x}_l \leq \boldsymbol{x} \leq \boldsymbol{x}_u, \end{aligned} \tag{3.1}$$

where $\boldsymbol{x}$ and $\boldsymbol{u}$ are the design variables and the state variables, respectively. The objective function is $f(\boldsymbol{x}, \boldsymbol{u})$ and $\boldsymbol{F}_i(\boldsymbol{x}, \boldsymbol{u})$ represents a vector that contains the constraints. The vector $\boldsymbol{R}(\boldsymbol{x}, \boldsymbol{u}) = 0$ is the governing equations. In the use of flutter, the governing equation is an eigenvalue problem. Note that within this research, displacement constraints were not imposed.

3.1.1 Objective function

Structural weight is one of the most important parameters in aircraft design, which greatly affects performance. It has been used as objective function in many other similar aircraft design optimization studies [Walsh et al., 2002, Eastep and McIntosh, 1968, Simodynes, 1974]. In this research, weight was used as the main objective function.

A finite element model will be constructed for structural analysis. The structure weight is a summation of the contributions from each element in the model. The mass of each elements will be calculated by the integration of each component using a Gauss quadrature scheme.

3.1.2 Design Variables

In this research, wing structure component thickness will be used as the design variables. Other parameters can also greatly affect structural weight, strength, and aeroelastic characteristics. For instance, the number of motors and their mounted locations. These parameters will not be treated as design variables in this optimization problem, but as system parameters. However, we can still change them to evaluate different configurations and determine their effect on aircraft design.

In the optimization process, the force the aerodynamic loading is equal to total structural weight multiplied by the load factor. For this reason, the angle of attach is also be treated as design variable in the practice optimization process.

3.1.3 Stress constraint

The constraints in the optimization problem include the structural constraint and the flutter constraint. The structural constraints require that the stress in each component of the structure should be within a certain bound in order to ensure structural safety.

The point-wise failure criterion is

$$F\left(\boldsymbol{x}_M, \boldsymbol{\epsilon}\right) \leq 1, \tag{3.2}$$

where $F\left(\boldsymbol{x}_M, \boldsymbol{\epsilon}\right) \in \mathbb{R}$ is a function that depends on material design variables $\boldsymbol{x}_M$, and local strain $\boldsymbol{\epsilon}$ [Jones, 1998]. Following this approach, the von Mises failure criterion can be written as follows:

$$F_{vM}\left(\boldsymbol{x}_M, \boldsymbol{\epsilon}\right) = \frac{\sigma_{vM}}{\sigma_{ys}} = \frac{1}{\sigma_{ys}}\sqrt{\sigma_x^2 + \sigma_y^2 - \sigma_x\sigma_y + 3\sigma_{xy}^2} \leq 1, \tag{3.3}$$

where σ_{ys} is specified stress.

3.1.4 Flutter constraint

The flutter constraint guarantees that flutter will not occur below a certain speed, such that the real part of the eigenvalues of the flutter governing equation must be no greater than zero. To ensure a sufficient margin is achieved, a safety factor is widely used in practice. With this safety factor, the flutter constraint can be written as follows:

$$\mathcal{R}\left(\boldsymbol{\xi}\left(v\right)\right) \leq -\rho,\ v_l \leq v \leq v_u, \tag{3.4}$$

where $\boldsymbol{\xi}$ is the eigenvalue which is a function of speed v, v_u is the chosen critical speed, and ρ is the safety factor which is a small number greater than zero.

The practical method adopted to check the flutter constraint in this research is to checking a set of points distributed along the speed interval between v_l and v_u. If the largest real part of all the eigenvalues at each speed point is less than the safety factor, it can be claimed that the flutter constraint is satisfied at the speed v_u, as seen Figure 3.1.

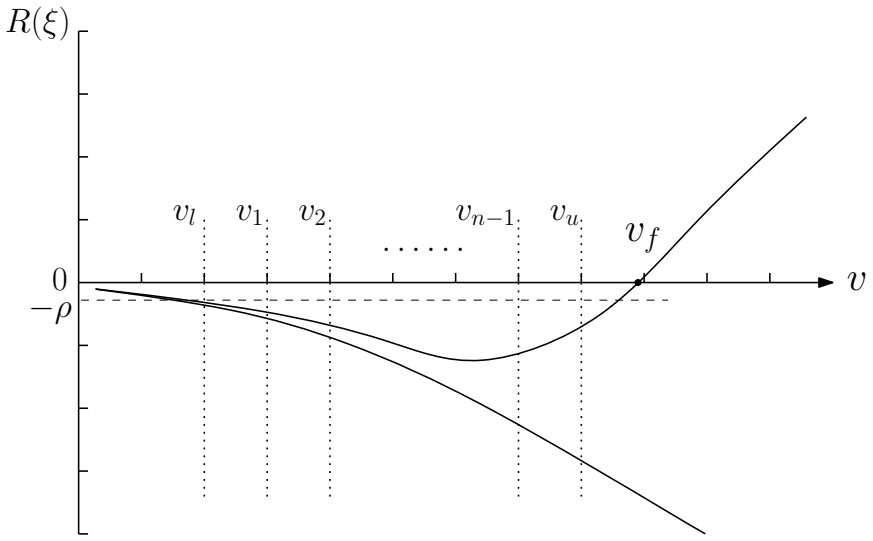

Figure 3.1: Approach to check flutter constraint at certain airspeed

3.1.5 Trim constraint

The aircraft trim constraint requires that the aerodynamic loading is equal to the aircraft's total weight multiplied by the load factor.

$$L = W \times n, \tag{3.5}$$

where L is the total aerodynamic loading which can be obtained from aerodynamic analysis, W is the total weight which usually listed in the aircraft technical specifications or can be estimated by empirical formula, and n is the load factor. The method to determine flight load factor will be introduced in following chapter.

3.2 Aerostructural analysis

A brief description of the coupled aeroelastic equations of motion for aeroelastic analysis is presented here. A descriptor expression of equations of motion is essential due to the presence of static constraints within the FEM. In this form, the time-derivatives of state variables will be treated as arguments of the governing equations. The fully coupled equation of motion can be express in residual form as follows [Kennedy et al., 2014],

$$\boldsymbol{R}\left(\boldsymbol{X}, \ddot{\boldsymbol{q}}, \dot{\boldsymbol{q}}, \boldsymbol{q}\right) = \boldsymbol{0}, \tag{3.6}$$

where $\boldsymbol{X}$ stands for design variables, and $\boldsymbol{q} = \left[\boldsymbol{u^T}, \boldsymbol{w^T}\right]^T$ are the state variables vector, which consists of the structural states variables $\boldsymbol{u}$ and the aerodynamic states variables $\boldsymbol{w}$; the symbols $\ddot{\boldsymbol{q}}$ and $\dot{\boldsymbol{q}}$ represent the derivatives of $\boldsymbol{q}$, respectively.

3.2.1 Structural analysis

The aim of the structural analysis is to calculate structural displacements and stress under aerodynamic loads. In this proposal, the structural analysis is conducted using TACS, a parallel finite-element code designed specifically for design optimization of stiffened, thin-walled composite structures using either linear or geometrically nonlinear strain relationships [Kennedy and Martins, 2014]. The residuals of the structural governing equations, can be written as follows [Kennedy et al., 2014]:

$$\boldsymbol{R}_S\left(\boldsymbol{x}, \boldsymbol{X}_S, \ddot{\boldsymbol{u}}, \dot{\boldsymbol{u}}, \boldsymbol{u}, \boldsymbol{w}\right) = \boldsymbol{M}\ddot{\boldsymbol{u}} + \boldsymbol{K}\boldsymbol{u} - \boldsymbol{F}_A = 0, \tag{3.7}$$

where $\boldsymbol{x}$ is the design variable vector, the matrix $\boldsymbol{M}$ is the mass matrix, the matrix $\boldsymbol{K}$ is the stiffness matrix, and the $\boldsymbol{F}_A$ is the nodal force.

3.2.2 Aerodynamic analysis

Aerodynamic analysis is used to estimate the aerodynamic loads exerted on structure. The aerodynamic analysis is conducted by using the Doublet-Lattice method. The discretized governing equations for the panel method can be written as follows:

$$\boldsymbol{R}_A\left(\boldsymbol{X}_A, \boldsymbol{w}\right) = \boldsymbol{A}\boldsymbol{w} - \boldsymbol{b} = \boldsymbol{0}, \tag{3.8}$$

where $\boldsymbol{A}$ is the aerodynamic-influence coefficient matrix, the vector $\boldsymbol{b}$ is a vector of boundary conditions, the upwash speed at each aerodynamic elements, $\boldsymbol{X}_A$ are the aerodynamic surface positions, and $\boldsymbol{R}_A$ is the aerodynamic residual.

3.2.3 Load and displacement transfer

To couple the aerodynamic and structural analysis, it is necessary to transfer displacements from the structure model to the aerodynamic model, and transfer loads from the aerodynamic model to the structural model. The displacement transfer is conducted as

$$\boldsymbol{X}_A = \boldsymbol{X}_A^0 + \boldsymbol{T}_A\boldsymbol{u}, \tag{3.9}$$

where $\boldsymbol{X}_A$ and $\boldsymbol{X}_A^0$ are the deformed and initial nodal locations of the aerodynamic surface, respectively. The matrix $\boldsymbol{T}_A$ is the transfer matrix,and $\boldsymbol{u}$ are the displacement of structure model. By integrating over the deformed aerodynamic surface, the nodal force [Kennedy et al., 2014] can be determined,

$$\boldsymbol{F}_A = \boldsymbol{F}_A\left(\boldsymbol{X}_s, \boldsymbol{X}_A, \boldsymbol{w}\right), \tag{3.10}$$

where $\boldsymbol{X}_S$ is the locations of structural nodes.

3.2.4 Coupled aeroelastic system

The fully coupled aeroelastic system of governing equations is obtained by combining the structural governing equation, Eq (3.7) with the aerodynamic governing equation, Eq (3.8).

$$\boldsymbol{R}\left(\boldsymbol{x}, \ddot{\boldsymbol{q}}, \dot{\boldsymbol{q}}, \boldsymbol{q}\right) = \begin{bmatrix} \boldsymbol{R}_A \\ \boldsymbol{R}_S \end{bmatrix}. \tag{3.11}$$

3.2.5 Flutter analysis

The flutter governing equation can be obtained by combining the structure governing equation and the aerodynamic governing equation, which can be written as follows:

$$\boldsymbol{M}\ddot{\boldsymbol{u}} + \boldsymbol{K}\boldsymbol{u} = \boldsymbol{F}\left(\ddot{\boldsymbol{u}}, \dot{\boldsymbol{u}}, \boldsymbol{u}\right), \tag{3.12}$$

where $\boldsymbol{M}$ and $\boldsymbol{K}$ are the mass and stiffness matrices, respectively, the $\boldsymbol{F}$ represents the aerodynamic forces and moments. The signs of the real parts of each eigenvalues of Eq. (3.12) will determine the flutter stability.

Apply the Doublet-Lattice method, the pressure coefficient difference between the upper and lower surface of the wing can be expressed as the following,

$$\boldsymbol{w} = \boldsymbol{A}^{-1}\left(\boldsymbol{b} - \boldsymbol{T}_A\dot{\boldsymbol{u}}\right), \tag{3.13}$$

where $\boldsymbol{T}'$ is the transpose of the transfer matrix. Steady aerodynamic loading will not affect the flutter stability, so only the unsteady part in the aerodynamic loading if of interest. According to the definition of the pressure coefficient, the flutter stability governing equations can be written as,

$$\boldsymbol{M}\ddot{\boldsymbol{u}} + \boldsymbol{C}\dot{\boldsymbol{u}} + \boldsymbol{K}\boldsymbol{u} = \boldsymbol{0}, \tag{3.14}$$

where

$$\boldsymbol{C} = \frac{1}{2}\rho U^2 \boldsymbol{T}_A' \boldsymbol{S} \boldsymbol{A}^{-1} \boldsymbol{T}_A.$$

Essentially, determining aircraft flutter stability is solving a second order polynomial eigenproblem. We can formulate the eigenproblem as below by assuming that $\boldsymbol{u} = \bar{\boldsymbol{u}}e^{\lambda t}$,

$$\lambda^2 \boldsymbol{M}\bar{\boldsymbol{u}} + \lambda \boldsymbol{C}\bar{\boldsymbol{u}} + \boldsymbol{K}\bar{\boldsymbol{u}} = \boldsymbol{0}. \tag{3.15}$$

The eigenvalue problem for the eigenvector $\mathbf{u} \in \mathbb{R}^n$ and eigenvalue $\lambda \in \mathbb{C}$ is solved

using the Jacobi-Davidson method for polynomial eigenvalue problems [Kennedy et al., 2014, Sleijpen et al., 1996, Sleijpen and Van der Vorst, 2000]. In order to simplify notation, $\bar{\boldsymbol{u}}$ is written as $\boldsymbol{u}$ in the following chapters.

CHAPTER 4

DEP AIRCRAFT OPTIMIZATION

This chapter contains details of the procedures and techniques utilized in the optimization process. First, the DEP wing model used in the optimization is described. Next, the tools for flutter analysis are described including the Doublet-Lattice method and the one-way propeller-wing aerodynamic coupling which estimates the aerodynamic loading. The coupling between aerodynamics and structures is performed using the Infinite Plane Spline (IPS), and the Jacobi-Davidson method used to solve the large-scale eigenproblem for the flutter constraint. Static aeroelastic analysis is performed using a coupled aeroelastic solution method that uses the Tripan aerodynamic analysis solver and the TACS structural solver. Finally, the HOpt optimizer which is used to solve the optimization problem, is described.

4.1 Aircraft coordinate system

The coordinate system adopted in this research is the same with most previous research and textbook. The x-axis is parallel with the wing root chord line, and points from the front of the aircraft to the tail. The y-axis lies along the wing-plane and points root to tip. The x, y, and z axes form a right-handed coordinate system.

4.2 Wing structure modeling

In this section, the construction of the wing structure model with the DEP configuration which will be used in the following optimization is shown. The LEAPTech aircraft is used as a reference during the construction of the wing model. Many geometry and performance parameters of LEAPTech aircraft are used. The advantage of using the parameters of an existing aircraft is that they can provide much practical and reasonable data as well as give better condition for possible benchmarking and comparison.

4.2.1 Parameters selecting

The first step is selecting parameter for the wing and electric motors mounted on it. Wing parameters mainly consist of wing geometric data such as airfoil type, wing span, aspect ratio, wing root chord length and so on. The airfoil of LEAPTech is based on the GA(W)-1 17% thickness airfoil designed from the ATLIT program [Holmes, 1977], and modified using MSES 2D multi-element airfoil design code to improve performance at the design takeoff and landing condition [Alex et al., 2014]. To simplify work in this research, the original GA(W)-1 17% airfoil was used without any further modification. Table 4.1 below contains detailed data on the parameters used.

Table 4.1: Detailed parameter for wing modeling

Parameter	Value	Parameter	Value
Aspect ratio	17.4	Root chord length	0.7 m
Taper ratio	0.481	Airfoil type	GA(W)-1 17%
Wingspan	9.0 m	Wing area	5.1m^2
Sweep angle	7.3^o	Dihedral angle	0^o

Mass, power, angular velocity or RMP, and tractive force are basic performance parameters of the electric motors. Apart from obtaining this data, the mounting positions for electric motors have to be determined. There will be a total of ten motors mounted on each semi-wing. The distances between each motor is the same. The symmetric axis of the propeller is parallel with the aircraft's x-axis. Figure 4.1 and 4.2 show the motor mounting position. Table 4.2 below contains detailed data. These parameters of the wing and motor form the foundation of following modeling steps.

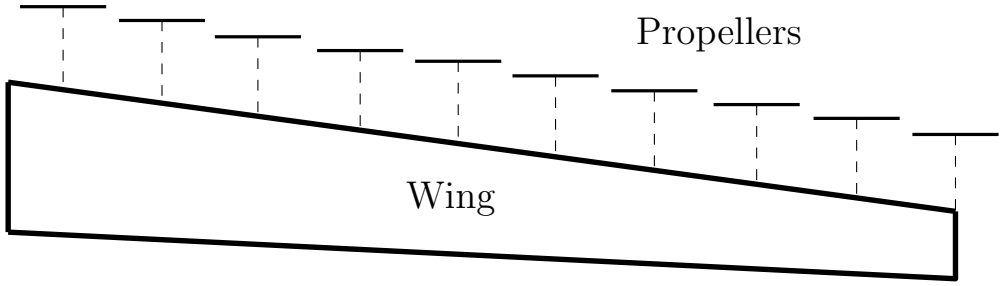

Figure 4.1: Motor mounting position (top view)

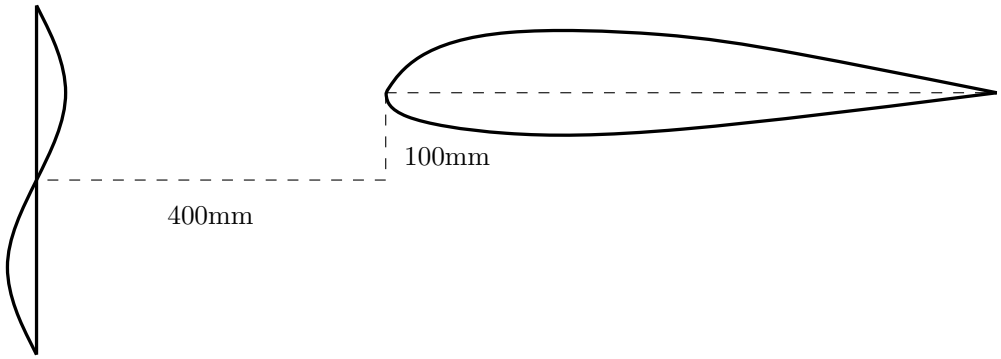

Figure 4.2: Motor mounting position (side view)

Table 4.2: Detailed parameter for electric motor

Parameter	Value
Propeller tip velocity	137.16 m/s
Total power	270 hp
Propeller radius	0.2 m
Propeller vertical distance below wing middle plane [1]	0.1 m
Propeller distance ahead of wing leading edge	0.4 m
Distance between first propeller and wing root	0.45 m
Distance between propellers	0.45 m

4.2.2 CAD and FEM modeling

The step after parameter selection is development of a CAD model and then generation of a corresponding finite-element model. Based on the parameters determined in last step, commercial software is utilized to construct the CAD model of the aerostructure. This CAD model is helpful in the next step, building the Finite Element Method (FEM) model. Moreover, visualizing the wing structure can help us in the design process to find potential inappropriate designs.

The FEM model of the wing is the foundation of structure analysis which will be used in the optimization process. In the FEM modeling, the main load-bearing component, the wing box consist of an upper and lower surface, front and rear beams and ribs is modeled. Only the semi-wing is necessary for analysis purpose, so the CAD and FEM both only contain

[1] the measurement point is the center of the propeller disks.

semi-wing and the grid on the symmetric plane is fixed as boundary condition in FEM model. Table 4.3 contains detail data. Figure 4.3 and Figure 4.4 show the result of CAD and FEM modeling.

Table 4.3: Detailed parameter for CAD and FEM modeling

Parameter	Value
front beam stand	0.0714
rear beam stand	0.7857
quantity of ribs	20
distance between ribs	225 mm

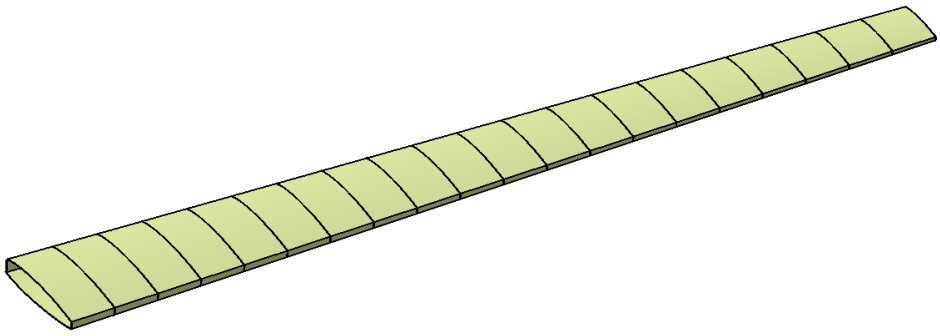

Figure 4.3: Aerostructure CAD model

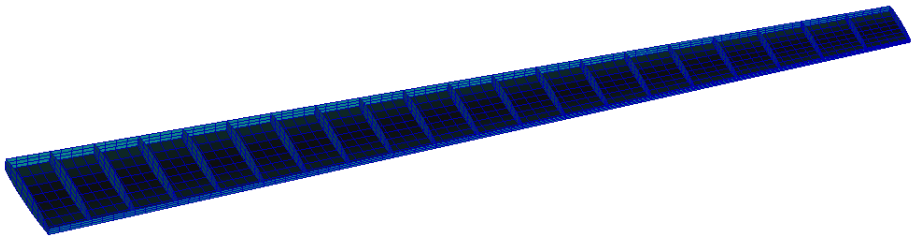

Figure 4.4: Aerostructure FEM model

4.3 Determining the flight condition

The result of the structure optimization would affect by the flight condition greatly. The reliability and credibility of the structure optimization is based on a realistic simulation flight condition. Also, the trim constraint requires determining the vertical flight load factor. In this section, the method or source to determine parameters of flight condition is presented. The flight condition obtained here includes critical airspeed, corresponding flight altitude, and vertical load factor.

4.3.1 Airspeed and altitude

In most simulation, the flight condition usually chosen is the level cruise stage which makes up most part of the flight scenarios [Pargett and Ardema, 2007]. The airspeed is usually the cruise speed and the flight altitude is commonly set as the cruise altitude. These two parameters are obtained by aircraft design requirements. Since this optimization model uses the LEAPTech DEP aircraft as a reference, it would be reasonable to use existing specifications to determine the flight condition. According to technical reports [Alex et al., 2014], these two parameters can be obtained, as seen in Table 4.4.

Table 4.4: Flight condition

Parameter	Value
airspeed	320 km/h
altitude	3650 m

4.3.2 Vertical load factor

The $V-n$ diagram depicts the aircraft limit load factor as a function of airspeed [Raymer, 2006, Anderson, 1999]. From this diagram, both the corresponding positive and negative maximum load factor under different airspeed can be obtained. Since the aerodynamic load can be classified into maneuver loads which result from common aerodynamic force, and the gust loads which occur when aircraft encounter strong gust, the $V-n$ diagram should have two separate courses to stand for these two kinds of loads. At each airspeed, the large load factor should be selected to guarantee flight safety.

Maneuver load

The maneuver load of an aircraft is determined by the maximum lift coefficient and expected use of the aircraft. At lower speed, the maximum available lift would limit the highest load factor that an aircraft can experienced. In other words, the maximum lift coefficient directly determines the maneuver load factor at lower speed.

$$n = \frac{\rho U^2 S C_{L_{max}}}{2W}, \tag{4.1}$$

where n is the load factor at lower speed, ρ is the air density at the altitude chosen before, S is the wing area, $C_{L_{max}}$ is the maximum lift coefficient, and W is the weight of the aircraft. We should be noted here that the U is the equivalent airspeed, which is defined as

$$U = \sqrt{\frac{\rho}{\rho_{SL}}} U_{actual}, \tag{4.2}$$

here ρ is the air density, ρ_{SL} is the air density at sea level, and U_{actual} is the actual airspeed.

At higher speeds, the maximum load factor is limited to a certain value based upon the expected use of the aircraft [Raymer, 2006]. From Table 4.5, the maximum positive and negative load factor at higher speed can be obtained [Raymer, 2006]. According to the class of the aircraft used in the optimization the possible maximum positive and negative load factors are 4 and -2 respectively, according to the use of the DEP aircraft, respectively.

Table 4.5: Flight condition

Usage	$n_{positive}$	$n_{negative}$
Transport	3 to 4	-1 to -2

In the computation of maneuver load, there are two special airspeed should be determined. The first critical speed is the cruise speed which is obtained from last section. The other critical speed is the maximum air speed and for subsonic aircraft, typically 40% to 50% higher than cruise speed is a reasonable estimation [Raymer, 2006].

Gust load

In some cases, the loads experienced can exceed the maneuver loads when the aircraft encounters a strong vertical gust. For a transport aircraft, this gust load factor can be as high

as negative 1.5 or positive 3.5 or more [Raymer, 2006].

An extra critical speed need to be determined in gust load estimation. The maximum turbulence speed V_g is specified in the design requirements. Here $0.7V_{cruise}$ as an estimator [Raymer, 2006].

The gust load factor can be estimate as follows,

$$\Delta n = \frac{\rho U V C_{L_\alpha}}{2W/S} \tag{4.3}$$

where V is the air speed, and C_{L_α} is the lift coefficient. The U is defined as,

$$U = KU_{de} \tag{4.4}$$

where U_{de} is the derived gust velocity which is specified in the design requirements. At cruise altitude, Table 4.6 below can be used to determine U_{de} [Raymer, 2006],

Table 4.6: Derived equivalent gust velocities

Flight speed	U_{de}
V_{max}	7 m/s
V_{cruise}	15 m/s
V_g	20 m/s

And,

$$K = \frac{0.88\mu}{5.3 + \mu} \tag{4.5}$$

μ is the mass ratio, defined as,

$$\mu = \frac{2W/S}{\rho g \bar{c} C_{L_\alpha}} \tag{4.6}$$

where $\bar{c}$ is the chord length. Noteworthy is that it can be assume the aircraft is conducting at level flight which means the maneuver load factor equals to one.

Combining these two load factors, the $V-n$ diagram can be plotted as shown in Figure 4.5

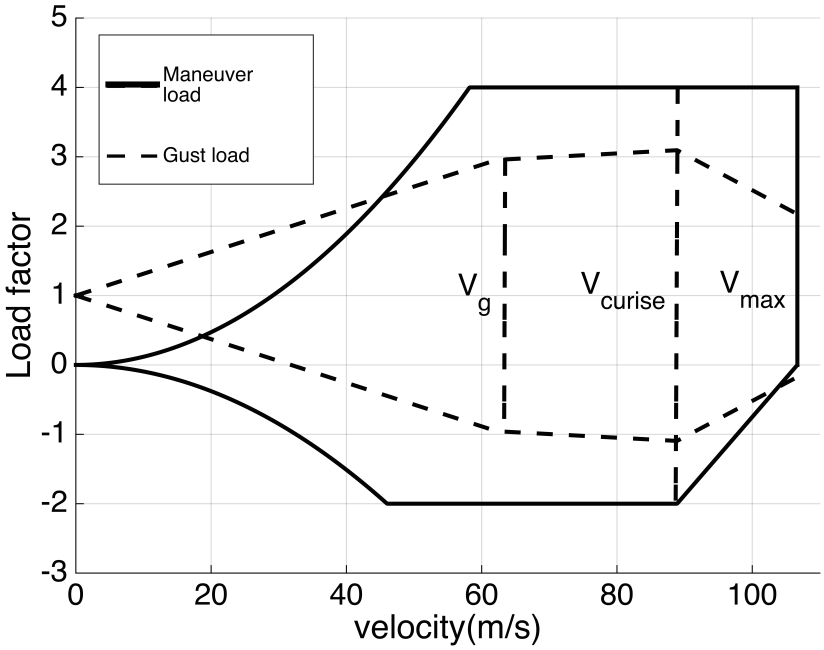

Figure 4.5: $V - n$ **diagram**

From the $V - n$ diagram, found that the maneuver load is much than gust load at most of the air speed range, especially at higher speed. The optimization flight condition is set to level flight at cruise speed. According to this figure, the maximum negative and positive load factor is set to -2 and 4, respectively.

In FAR part 23, these is a requirement that the selected positive load factor should no less than,

$$n = 2.1 + \frac{24000}{W_p + 10000}, \tag{4.7}$$

here W_p is maximum takeoff weight in pound. This limitation load factor for the LEAPTech aircraft is 3.946. The limitation of negative load factor is 0.5 times the positive load factor limitation. Obviously, the flight selected load factor satisfy the FAA Regulation.

4.4 The flutter constraint

The flutter constraint require the aerostructure is free from flutter phenomenon within a certain airspeed. to evaluate the flutter constraint is to solve a second order generalized eigenproblem derived from aerodynamics structure coupling system governing equation which is shown in chapter three. In this section, techniques and tools utilized to determine the flutter constraint are presented.

There are three main parts in this section. The first two parts presents the estimation of the aerodynamic load which will form the damping matrix in the flutter constraint eigenproblem. The Doublet-Lattice method and the Actuator disk theory are used to estimate the aerodynamic load and propeller-wing coupling effect. After forming the damping matrix, with the mass and stiffness matrix, the eigenproblem which determining whether the flutter constraint is satisfied can be formed. However, in real would practice, dimension of this eigenproblem usually can be large since it is proportional with the grid number in FEM model, and in order to accurately present structure dynamic characteristic, grid quantity usually is large. Coping with this computational difficulty, the technique introduced in the last part was utilized.

The last part introduces the Jacobi-Davidson method which used to solve the large dimensional flutter constraint. Instead of reducing the dimension of the problem which has been adopted by many previous research, this technique can produce the eigenvalues which are of greater interests. In this way it can be determined whether the flutter phenomenon occurs. The way to compute the gradient of the critical eigenvalue with respect of design variables is also presented.

4.4.1 The Doublet-Lattice method

In this research, the Doublet-Lattice method (DLM) that estimates aerodynamic force in the optimization procedure was applied. The DLM can be applied for oscillating lifting surfaces in subsonic flow. This theory has been presented by numerous authors [Albano and Rodden, 1969, Blair, 1992]. Linerized aerodynamic potential theory is the theoretical basis of the DLM.

Each aerodynamic surface or panel is divided into trapezoidal elements. These elements are required to be arranged in strips parallel to the free stream velocity. The unknown pressure differences of the upper and the lower wing surface are assumed to be exerted uniformly across the one-quarter chord line of each element. The upwash velocity of each element is computed at the collocation point which locates on the three-quarter chord line of the element. And the upwash velocity should satisfy the boundary condition obtain by incoming flow velocity and wing surface geometry [Rodden and Johnson, 1994]. By solving the linear equations below, the pressure differences for each boxes can be determined. Figure. 4.6 shows the aerodynamic mesh used in this research.

$$\boldsymbol{R}_A = \boldsymbol{A}\boldsymbol{w} - \boldsymbol{b} = \boldsymbol{0}. \tag{4.8}$$

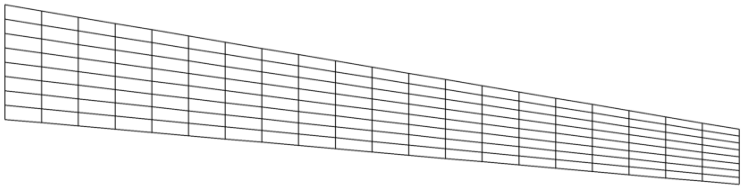

Figure 4.6: The mesh for aerodynamic analysis

Numerical estimation of integral I_1 and I_2

In the calculation process of the DLM, there are some integrals which are very hard to evaluated theoretically. Albano and Rodden introduced an estimation by approximate the integral function by combination of fundamental functions [Albano and Rodden, 1969]. I computed other similar integrals by this approximative approach.

Calculation of integral I_1 and I_2 is critical to determine the correct aerodynamic influence coefficient matrix. Expressions of these two integrals are

$$I_1 = \int_{u_1}^{\infty} \frac{e^{-ik_1 u}}{(1+u^2)^{3/2}}\,\mathrm{d}u \tag{4.9}$$

$$I_2 = \int_{u_1}^{\infty} \frac{e^{-ik_1 u}}{(1+u^2)^{5/2}}\,\mathrm{d}u, \tag{4.10}$$

where $u_1, \mathrm{and} k_1$ are real parameters. To reduce the computational time, approximating the integral by simple functions is preferred. It is sufficient to consider non-negative arguments because both of these two integrals have symmetry properties. Albano and Rodden [Albano and Rodden, 1969] introduced a method to approximate I_1. Integrating Eq. (4.9) by parts gives

$$I_1 = \left[1 - \frac{u_1}{(1+u_1^2)^{1/2}}\right] e^{-ik_1 u_1} - ik_1 \int_{u_1}^{\infty} \left[1 - \frac{u}{(1+u)^2}\right] e^{-ik_1 u}\,\mathrm{d}u, \tag{4.11}$$

and we have the approximation formula

$$\frac{u}{(1+u^2)^{1/2}} \approx 1 - 0.101e^{-0.329u} - 0.899e^{-1.4067u} - 0.09480933e^{-2.9u}\sin(\pi u)\,, u \geq 0. \tag{4.12}$$

By substituting Eq. (4.12) into Eq. (4.11), we can obtain an expression for I_1 that can easily be evaluated. Following this approach, a similar approximation formula for I_2 can be

developed. Integrating Eq. (4.10) by parts gives

$$I_2 = \left[\frac{2}{3} - \frac{3u_1 + 2u_1^3}{3\left(1+u_1^2\right)^{3/2}}\right] e^{-ik_1 u_1} + ik_1 \int_{u1}^{\infty} \left[\frac{3u + 2u^2}{3\left(1+u^2\right)^{3/2}} - \frac{2}{3}\right] e^{-ik_1 u}\, \mathrm{d}u, \tag{4.13}$$

and the result of the approximation formula is obtained by utilizing Matlab® curve fitting toolbox,

$$\frac{3u + 2u^3}{3\left(1+u^2\right)^{3/2}} = \frac{2}{3} - 0.5545e^{2.011u} - 0.1122e^{-2.013u} - 0.9348e^{-6.291u}\sin(\pi u)\,, u \geq 0. \tag{4.14}$$

These expression allow the integrals of I_1 and I_2

The DLM validation & verification

To verify the DLM code, it is necessary to compare the result of the DLM with experimental data or numerical results presented in other papers.

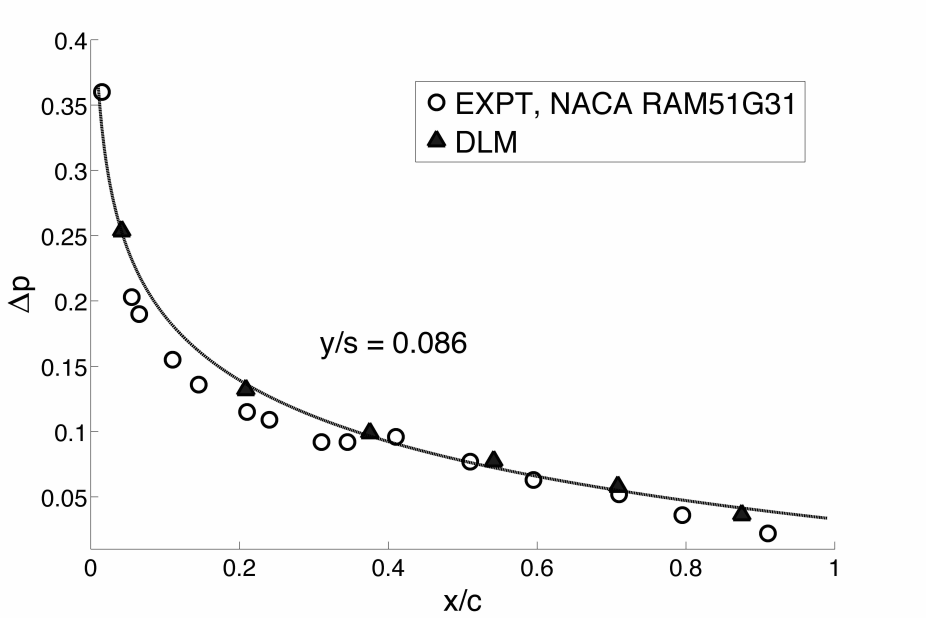

Figure 4.7: Lift distribution on swept wing in steady flow, y/$s = 0.086$

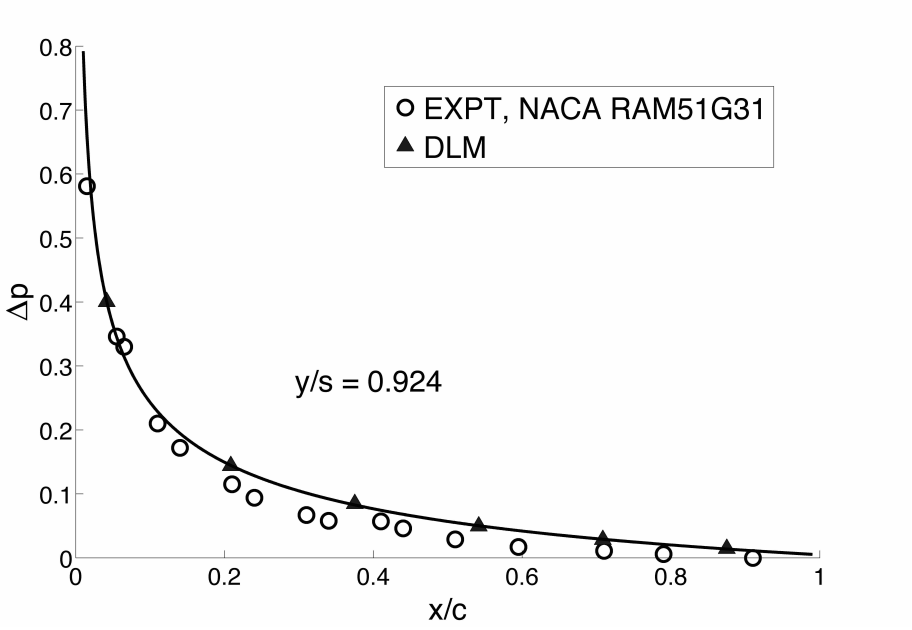

Figure 4.8: Lift distribution on swept wing in steady flow, y/$s = 0.924$

For the steady flow, the lift distribution of a wing is calculated with an aspect ratio of 3, sweep angle of 45°, taper ratio of 0.5, a Mach number of 0.25, and an angle of attack of 2°. Kolbe and Boltz [Kolbe and Boltz, 1951] measured and reported experimental lift distribution data in 1951. For this problem, the semi-wing was divided into 6×17 elements. Each sending and receiving point is located at the $\frac{1}{4}$-chord and $\frac{3}{4}$-chord, respectively, of each box. Figure 4.7 and Figure 4.8 shows this comparison. Figure 4.9 shows the pressure coefficient distribution of the wing.

For the condition of unsteady flow, lift distributions of a square aerodynamic surface under oscillating upwash velocity were calculated. This surface is divided into 3×3 elements. The calculated result of the same configuration surface is reported by Blair [Blair, 1992]. Table 4.7 presents a comparison between the results reported by Blair and the present code. The maximum discrepancy is 1.7%.

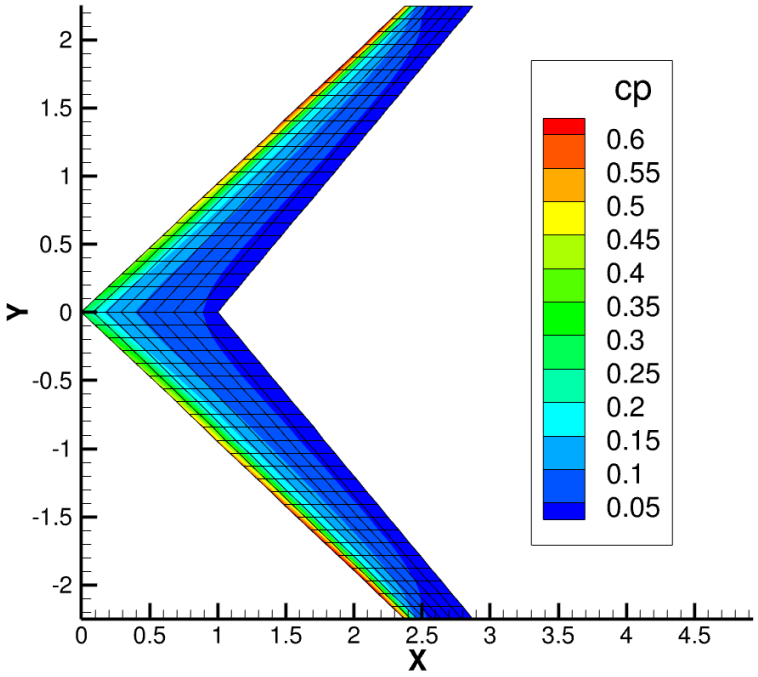

Figure 4.9: Pressure coefficient distribution of the wing

Table 4.7: Lift distribution for oscillating surface

Box index	Result from Blair	Result from author
0	$-0.5490 + 6.2682i$	$-0.5415 + 6.2603i$
1	$-3.8862 + 2.4495i$	$-3.8815 + 2.4489i$
2	$-3.8736 + 1.1745i$	$-3.8720 + 1.1746i$
3	$-0.5914 + 5.8092i$	$-0.5851 + 5.8025i$
4	$-3.6405 + 2.1530i$	$-3.6364 + 2.1526i$
5	$-3.6234 + 1.0281i$	$-3.6220 + 1.0281i$
6	$-5.8286 + 4.5474i$	$-0.5785 + 4.5432i$
7	$-2.8983 + 1.4663i$	$-2.8957 + 1.4660i$
8	$-2.8893 + 7.1186i$	$-2.8883 + 0.7118i$

4.4.2 One way propeller-wing coupling

The aerodynamic coupling between propellers mounted along the lead edge and wing affects DEP aircraft performance greatly. This is where the high aerodynamic efficiency advantage of DEP aircraft comes from. Taking a closer look of the coupling mechanism, the propwash will cause changes in the local upwash velocity at the collocation points defined in

the Doublet-Lattice method on the wing, which will modify the aerodynamic forces. For example, the axial flow after propellers can increase airspeed over the wing section which is equivalent to the increase the flight speed, and thus enlarges the lift. With this interaction, DEP aircraft can achieve high maximum lift coefficient $C_{L_{max}}$. For instance, the LEAPTech aircraft discussed in the previous chapter is able to have a $C_{L_{max}}$ as large as 5.0 or more [Alex et al., 2014].

The actuator disk theory

The propeller induced velocity profile can be estimated by the propeller actuator disk theory, which also known as the momentum theory [Conway, 1995]. The actuator disk theory has been used in both the aeronautical and hydronautical industries for years to calculate the velocity fields induced by an actuator disk [Stern et al., 1986, Strash et al., 1984].

In the actuator disk theory, the induced perturbations to the stream flow are contributed to by four vertex distributions [Conway, 1995], as seen in Figure 4.10 and 4.11. These are:

1. a vortex tube consisting of ring vortices distributed over a tube shed from the edge of the actuator disk and extending to downstream infinity;
2. the constant strength hub vortex along the axis of symmetry and extending to downstream infinity;
3. a distribution of radial vorticity on the actuator disk;
4. a surface distribution of vorticity on the slipstream surface.

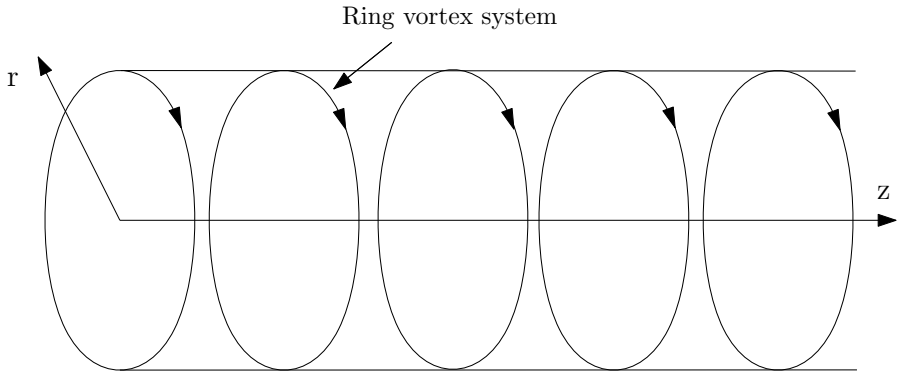

Figure 4.10: Vortex system induces the axial and radial velocities

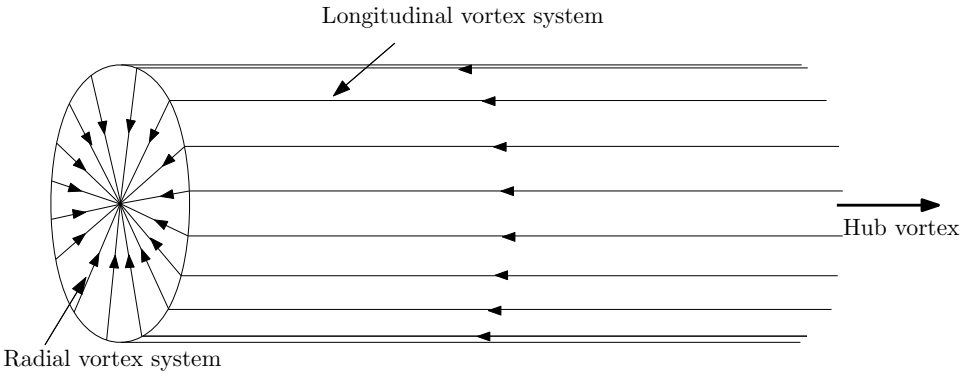

Figure 4.11: Vortex system induces the azimuthal velocity

On the condition that the propeller has a elliptic loading, the solution of the actuator disk theory can be stated in terms of elementary functions [Conway, 1995]. By utilized standard Bessel integrals introduced by Gradshteyn and Ryzhik [Gradshteyn et al., 2000], we have,

$$V_r\left(r,z\right)=\frac{V_{z0}\left|z\right|}{2r}\left(\frac{1}{\alpha}-\alpha\right)-\frac{V_{z0}r}{2R_a}\arcsin\beta, \tag{4.15}$$

$$V_z(r,z)=2V_r\left(r,0\right)+V_{z0}\left(-\alpha+\frac{z}{R_a}\arcsin\beta\right),\quad\left(z>0\right), \tag{4.16}$$

where r and z equals the distance from the symmetric axis and the actuator disk, respectively. R_a is the radius of the propeller. And the $V_z\left(r,0\right)$, α and β is defined as,

$$V_z\left(r,0\right)=\frac{V_{z0}}{R_a}\left(R_a^2-r^2\right)^{1/2}, \tag{4.17}$$

$$\alpha=\left\{\frac{\left[\left(R_a^2-r^2-z^2\right)^2+4R_a^2z^2\right]^{1/2}+R_a^2-r^2-z^2}{2R_a^2}\right\}^{1/2}, \tag{4.18}$$

$$\beta=\frac{2R_a}{\left[z^2+\left(R_a+r\right)^2\right]^{1/2}+\left[z^2+\left(R_a-r\right)^2\right]^{1/2}}, \tag{4.19}$$

The V_{z0} is the axial velocity at the center of the actuator disk and appears in almost every equation above. It can be determine using following approach. At the actuator disk, considering the linear limit, the pressure discontinuity across the actuator disk can be expressed as,

$$\Delta P\left(r\right)=2\rho U_\infty V_z\left(r,0\right), \tag{4.20}$$

and the expression of $V_z\left(r,0\right)$ is Eq. (4.17). Integral all over the actuator disk can yield the

thrust P providing by the propeller,

$$P = \int_0^{2\pi} \int_0^{R_a} \Delta P\left(r\right) r \mathrm{d}r \mathrm{d}\theta = \frac{4\pi\rho U_\infty V_{z0} R_a^2}{3}, \tag{4.21}$$

by Eq. 4.21, we form a relationship between velocity V_{z0} and the propeller thrust which can be obtain easily.

The azimuthal velocity can be determined using the following approach [Conway, 1995],

$$V_\phi\left(r, z\right) = \frac{\Gamma_s\left(r\right)}{2\pi r}, \tag{4.22}$$

where $\Gamma_s\left(r\right)$ is the total axial flux of vorticity within radius r fo the axis of symmetry, and it can be calculated with the following relationship,

$$\Gamma_s\left(r\right) = \frac{4\pi V_z\left(r, 0\right)\left(U_\infty + V_z\left(r, 0\right)\right)}{\Omega}, \tag{4.23}$$

where Ω is the propeller rotating angular velocity.

Coupling propeller with wing

The one way coupling between the propeller and wing is achieved by superimposing the induced velocity profile calculated by the actuator disk theory with the Doublet-lattice method. The induced velocity will change the local upwash speed at the control points. Figures 4.12 and 4.13 show that the area the propeller affects is a tube behind the propeller disk.

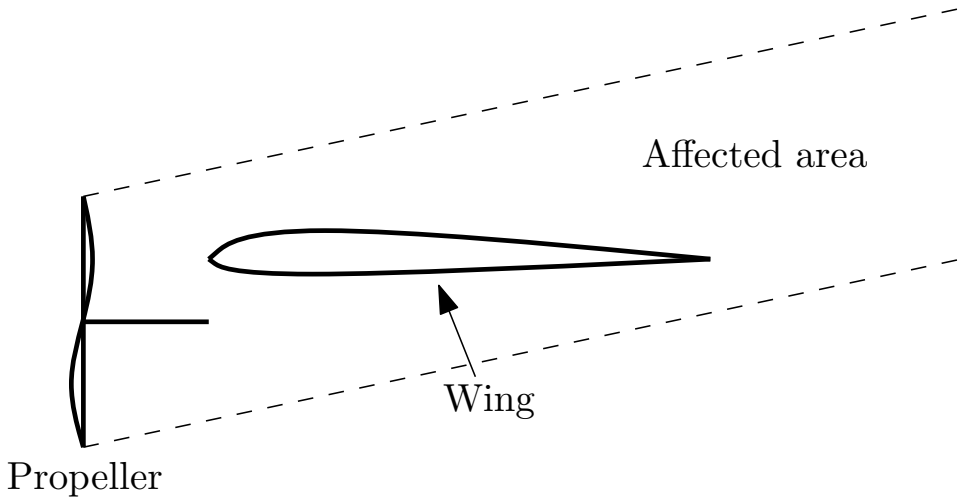

Figure 4.12: Propeller influence region (side view)

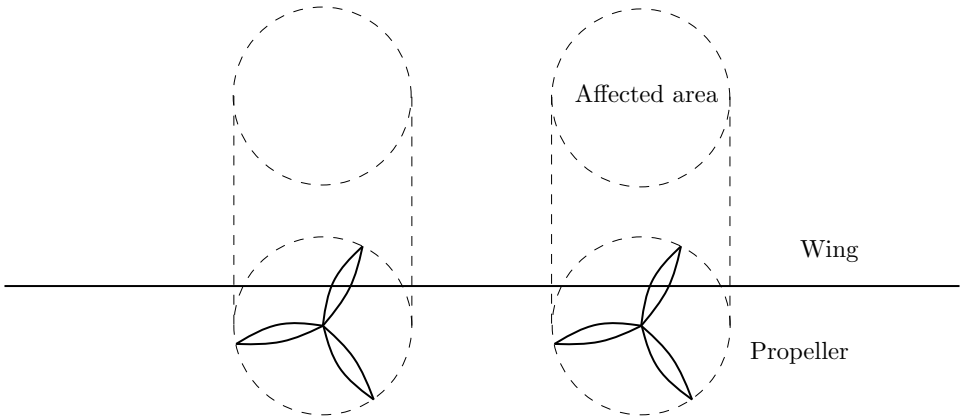

Figure 4.13: Propeller influence region (front view)

Next, the computational result of propeller and wing one way coupling is presented. This one-way coupling technique was applied to the aerodynamic mesh built in previous section 4.6. There are eight elements in the chord direction and twenty elements in the span direction. The flight condition parameters and motor specifications are shown in the Table 4.8 below. These parameters are determined by referring to the cruise flight condition introduced in the LEAPTech aircraft technical report [Alex et al., 2014].

Table 4.8: Flight condition and motor parameters of propeller-wing one way coupling computation

Flight condition and motor parameter	values
Airspeed	320 km/hr
Altitude	3650 m
Angle of attack	1^o
Total thrust	3100 N
Propeller tip velocity	137 m/s

With these parameters, the coupling effect between the wing and propeller can be computed and the effect on aerodynamic performance analyzed. Figure 4.14 and Figure 4.15 show the difference between the pressure coefficient and upwash velocity distribution with and without propeller interaction. According to this result, the propeller induced velocity field would increase axial velocity all over the wing, and also have some waving distribution spanwise because of propeller induced flow tangential component. The overall effect on the aerodynamic performance is that the interaction increases the wing lift coefficient, as seen

in Table 4.9. Note that the predicted increasing in the lift coefficient is 40.7%.

Table 4.9: Propeller-wing interaction on left coefficient

	Without propeller	With propeller
Total lift (kg)	16887	23623
Lift coefficient	0.68	0.975

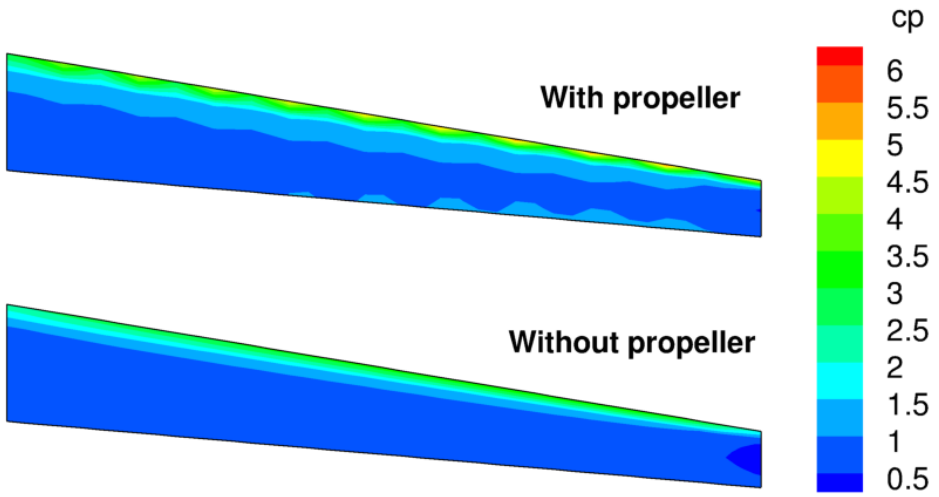

Figure 4.14: C_p distribution with/without propellers

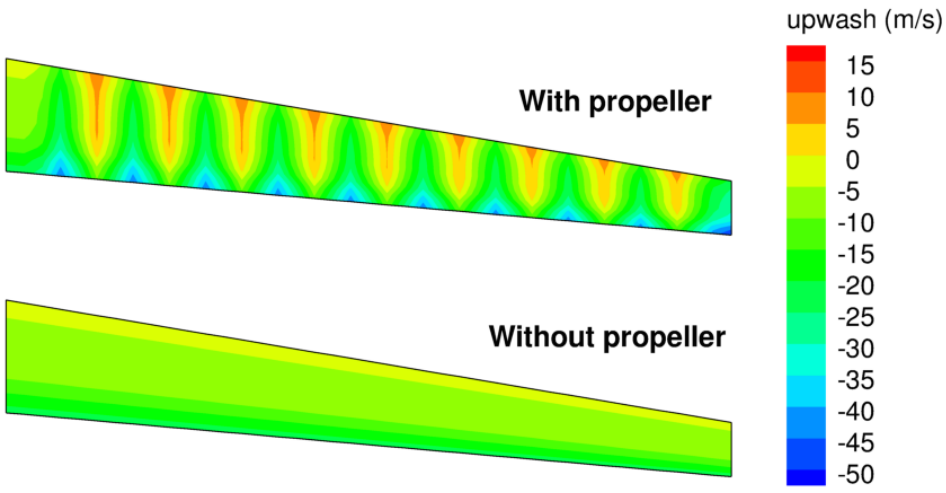

Figure 4.15: Upwash velocity distribution with/without propellers

4.4.3 IPS load & displacement transfer method

A load and displacement transfer scheme was employed to transfer the aerodynamic loads to the structural model and to extrapolate the displacements from the structural model to the aerodynamic surface. IPS is one of the most popular methods of interpolation [Smith et al., 2000, Jaiman et al., 2011] and has first introduced by Harder [Harder and Desmarais, 1972]. Program such as ASTROS and MSC.Nastran currently use this method. The IPS method is based on a superposition of the solution of the partial differential equation for an infinite-plate. The advantages of this method are that the interpolated function is differentiable everywhere and the grid is not restricted to a rectangular array[Smith et al., 2000].

This method was applied on the function $W(x, y) = (1 + 9x^2 + 16y^2)^{-1}$, where x and y is the Cartesian coordinate, W is the displacement. The base mesh contains a 11×11 grids while the spline mesh contains a 21×21 grid. The result is present below, see Figure 4.16. The maximum absolute relative error is 2.1%.

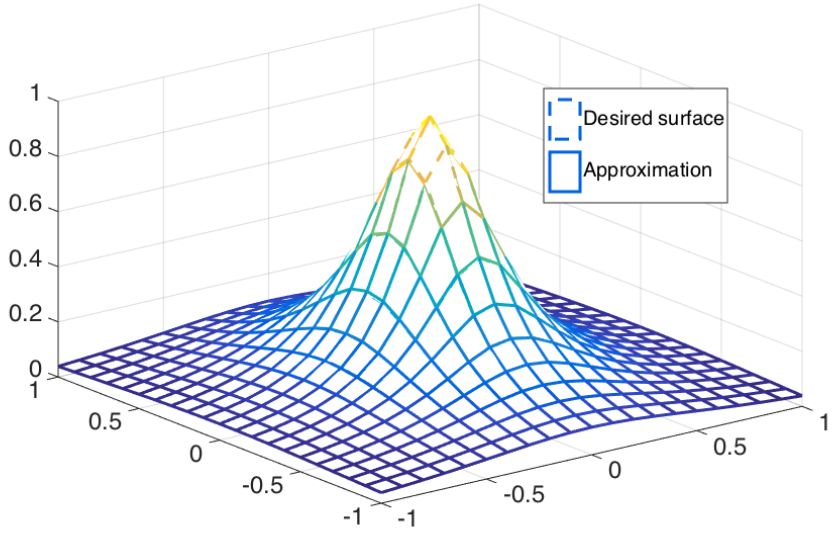

Figure 4.16: IPS verification of a bell shape surface

4.4.4 Propellers and motors dynamic modeling

The propellers and motors mounted on the leading edges may not only affect the aerodynamic performance of the wing, but may also impact the wing structure dynamic characteristics. Four factors are considered in this research.

Propellers thrust

Propeller would produce thrust at its mounted point and the direction is parallel with the symmetric axis of the propeller. Since the wing structure is elastic and may have deflection under aerodynamic loading, the direction of thrust can also change with the structural deformation which makes thrust behave as a "follower force". Many outstanding work has been done previously. Hodges, Patil and Chae conducted a detailed research about the impact of follower force on flutter stability[Hodges et al., 2002]. Whether or not thrust is stabilizing depends strongly on the ratio of bending stiffness to torsional stiffness η. For $\eta \leq 5$, it was shown that thrust up to a certain value can increase flutter speed. But for $\eta \geq 10$, thrust always decreases flutter speed.

DEP aircraft usually have large aspect ratios, so the wing structure of DEP aircraft is flexible compared with conventional wings. Furthermore, instead of a small number of installed propellers, DEP aircraft may have more than ten propellers mounted on the wing. For instance, the LEAPTech aircraft has twenty propellers mounted at the same time. For these reasons, it is important to investigate how will this factor will affect the wing structure characteristics including flutter stability. An illustration of the propeller thrust coupling with wing structural model is depicted in Figure4.17

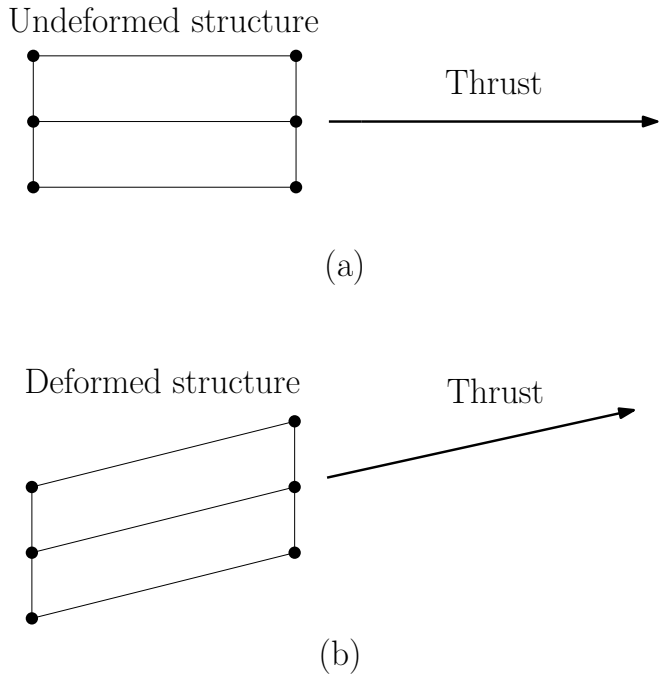

Figure 4.17: Structural deflection changes direction of thrust. (a). Undeformed strucutre with the thrust (b). deformed structure makes thrust point different direction

To account for this following force in the flutter constraint, a non-symmetric following force term was added in the governing equations. The general form of follower force can be expressed as

$$\boldsymbol{F}_f = \boldsymbol{F} + \boldsymbol{\theta} \times \boldsymbol{F}, \tag{4.24}$$

$\boldsymbol{F}_f$ is the follower force, $\boldsymbol{F}$ is the original tractive force provided by propeller, $\boldsymbol{\theta}$ is a deformation angle. A 2-D case of follower force is presented below. Since the flutter dynamic equation Eq. (3.12) only considers the vertical movement, only the vertical component of the thrust has an impact on this equation. To evaluate the change of thrust direction, a structural model node is picked and compute its relative displacements. Once obtained, vertical thrust component is computed and added it to the governing equation. With simply computation, two nodes on the propeller symmetric axis when the structure is undeformed are used to compute the thrust direction change shown Figure 4.18.

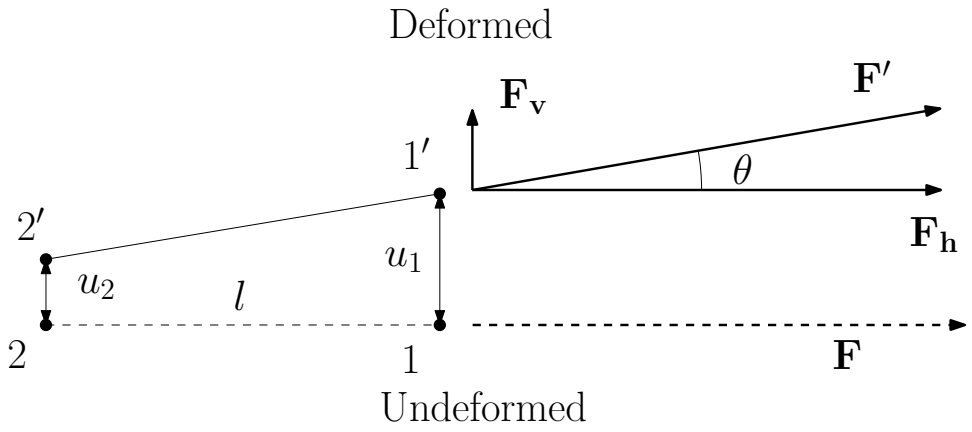

Figure 4.18: Determing thrust vertical component

In Figure4.18, the structural model node 1 and 2 moves to location $1'$ and $2'$ and have vertical displacement u_1 and u_2 under loading, respectively. l is the horizontal distance between them. The thrust pitch from $\boldsymbol{F}$ to $\boldsymbol{F}'$, $\boldsymbol{F}_v$ and $\boldsymbol{F}_h$ are the vertical and horizontal component of the thrust, respectively, and θ is the angle between thrust and its horizontal component. The thrust vertical component $\boldsymbol{F}_v$ can be expressed as following,

$$\boldsymbol{F}_v = \hat{\boldsymbol{n}}_z |\boldsymbol{F}| \sin\theta, \tag{4.25}$$

where $\hat{\boldsymbol{n}}_z$ is the vertical direction unit vector. In order to include the coupling into the flutter

eigenproblem, the following simplification is necessary,

$$\boldsymbol{F}_v = \hat{\boldsymbol{n}}_z |\boldsymbol{F}| \tan\theta = \hat{\boldsymbol{n}}_z |\boldsymbol{F}| \frac{u_1 - u_2}{l}. \tag{4.26}$$

The relative error between $\tan\theta$ and $\sin\theta$ is less than 0.5% while the θ is less than 5^o. And the angular deformation is smaller than that. So this approximation here is valid. According to Equation (4.26), the thrust vertical component can be coupled into the flutter eigenproblem as follows,

$$\boldsymbol{M}\ddot{\boldsymbol{u}} + \boldsymbol{C}\dot{\boldsymbol{u}} + \boldsymbol{K}\boldsymbol{u} = \boldsymbol{P}\boldsymbol{u} = \begin{bmatrix} & \vdots & & \vdots & \\ \cdots & \pm\dfrac{F_i}{l_i} & \cdots & \mp\dfrac{F_i}{l_i} & \cdots \\ & \vdots & & \vdots & \end{bmatrix} \boldsymbol{u}. \tag{4.27}$$

Matrix $\boldsymbol{P}$ has the same size with those matrices on the left hand side. Moving the right hand side term in Equation (4.27) to the left will yield the coupling governing equation,

$$\boldsymbol{M}\ddot{\boldsymbol{u}} + \boldsymbol{C}\dot{\boldsymbol{u}} + (\boldsymbol{K} - \boldsymbol{P})\,\boldsymbol{u} = \boldsymbol{M}\ddot{\boldsymbol{u}} + \boldsymbol{C}\dot{\boldsymbol{u}} + \boldsymbol{K'}\boldsymbol{u} = \boldsymbol{0}. \tag{4.28}$$

Although follower force may make impact on flutter stability, it has no been coupled into flutter constraint yet because some difficulties. However, the effect on the stress constraint will be examined in a later chapter.

Gyroscopic moment

The gyroscopic moment comes from the rotating propellers and motor shafts. The expression for the gyroscopic moment exerted on the structure is

$$\boldsymbol{M}_k = \boldsymbol{H} \times \boldsymbol{\omega}, \tag{4.29}$$

where $\boldsymbol{M}_k$ is the gyroscopic moment, $\boldsymbol{H}$ is the rotation moment of momentum, $\boldsymbol{\omega}$ is the movement angular velocity. Assuming that the symmetric axes of propellers and motor shafts are placed parallel with x axis of the aircraft. In this research, ignoring the wing section twist deformation, the propellers and motor shafts both rotates clockwise when the observer is in front of the aircraft. Therefore, the direction of $\boldsymbol{H}$ is parallel with x axis of the aircraft and points from the aircraft head to tail. Since the vertical movement is included in the flutter analysis, the direction of $\boldsymbol{\omega}$ is parallel with y axis of the aircraft. According to Equation.4.29, the direction of the gyroscopic moment is parallel with z axis of aircraft, as

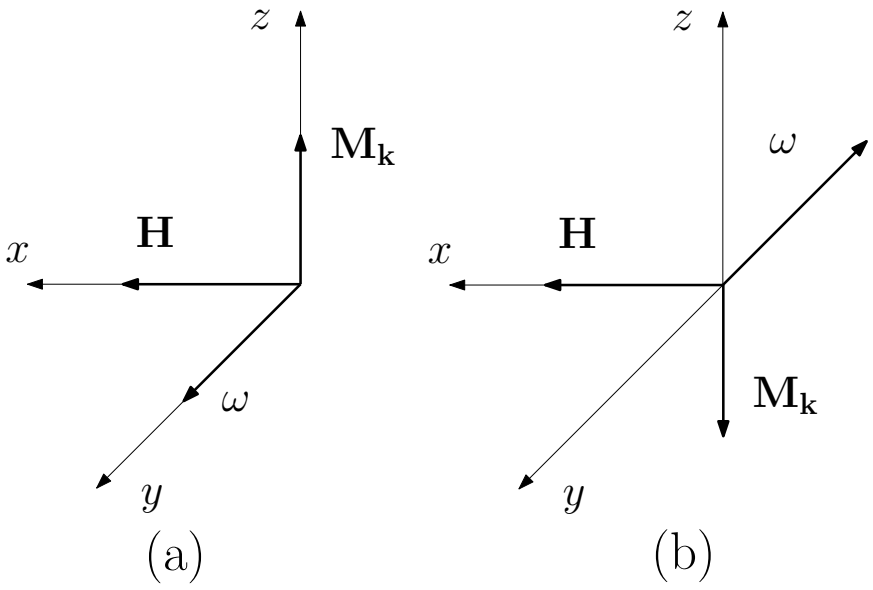

Figure 4.19: Gyroscopic moment direction

depicted Figure 4.19.

Since the gyroscopic moment is always perpendicular with the wing middle plane, no matter what the direction of the movement angular velocity, the gyroscopic moment has little impact on wing structure banding movement. Therefore, the gyroscopic moment is not considered in the flutter stability constraint. However, movements involving wing twist deformation may make the gyroscopic moment interact with the bending motion, but this higher order factor is not essential for this work.

Shaft moment

Assume the propeller spins at constant angular velocity, because of aerodynamic drag on the blades, it will generate a torque on the wing structure which direction is opposite with the propeller angular velocity. However, ignoring the wing section twist deformation, this counter torque is constant and static which will not affect aircraft flutter stability. So this factor is omitted in the flutter analysis.

Propellers and motors inertia

In order to simplify the analysis, the propellers and motor just be considered as a mount of mass at their center of mass. The inertia effect of the propeller and motor can be coupling into model by adding elements at each center of mass which just has mass but not provide any stiffness to the FEM model.

4.4.5 The Jacobi-Davidson method

Flutter stability is governed by a second order polynomial eigenproblem. Once the eigenvalues of this eigenproblem are obtained, the flutter stability can be determined by checking the signs of real part of every eigenvalue. This research applied the Jacobi-Davidson method [Sleijpen and Van der Vorst, 2000, Sleijpen et al., 1996] and it can be applied directly to the polynomial eigenproblem written as below,

$$\left(\lambda^2 \boldsymbol{J}_2 + \lambda \boldsymbol{J}_1 + \boldsymbol{J}_0\right) \boldsymbol{u} = \boldsymbol{0}. \tag{4.30}$$

The Jacobi-Davidson method is based on two known ideas [Sleijpen and Van der Vorst, 2000, Sleijpen et al., 1996]. The first is solving eigenproblem approximately by projecting the problem onto a low-dimensional search subspace. This can be interpreted as the Davidson part of this method. If the dimension of the search subspace is small, eigenproblem can be solved efficiently. The search subspace must built in such a way that it contain a basis for the desired eigenpair. In a 1846 paper, Jacobi expended the basis of the search subspace by approximately solving a linear system of equation to obtain the correction step. For stability reasons, the basis of the search subspace should be orthonormalized. If the correction step is solved to a sufficient degree of accuracy, the asymptotic rate of convergence to an eigenpair is quadratic. The Jacobi-Davidson algorithm is outlined below [Saad, 1992],

1. Start:
   (a) Choose an initial subspace $\boldsymbol{V}$
   (b) Orthonormalize $\boldsymbol{V}$
2. Repeat:
   (a) Compute $\boldsymbol{H}_i \leftarrow \boldsymbol{V}^H \boldsymbol{J}_i \boldsymbol{V}, i = 0, 1, 2.$
   (b) Compute desired eigenpair $(\theta, \boldsymbol{y})$ of a smaller dimension problem

$$\left(\theta^2 \boldsymbol{H}_2 + \theta \boldsymbol{H}_1 + \theta \boldsymbol{H}_0\right) \boldsymbol{y} = \boldsymbol{0}, \tag{4.31}$$

   where $\|\boldsymbol{y}\| = 1$, then compute $\boldsymbol{u} \leftarrow \boldsymbol{V}\boldsymbol{y}$, $\boldsymbol{w} \leftarrow 2\theta \boldsymbol{J}_2 \boldsymbol{u} + \boldsymbol{J}_1 \boldsymbol{u}$.
   (c) Compute residual

$$\boldsymbol{r} \leftarrow \boldsymbol{P}(\theta)\boldsymbol{u}, \tag{4.32}$$

   where $\boldsymbol{P}(\theta) = \theta^2 \boldsymbol{C}_2 + \theta \boldsymbol{C}_1 + \boldsymbol{C}_0$. Stop process if satisfy convergence criteria.

(d) Solve for the correction step approximately by apply GMRES algorithm[Saad and Schultz, 1986],

$$\left(\boldsymbol{I}-\frac{\boldsymbol{w}\boldsymbol{u}^H}{\boldsymbol{u}^H\boldsymbol{w}}\right)\boldsymbol{P}(\theta)\left(\boldsymbol{I}-\boldsymbol{u}\boldsymbol{u}^H\right)\boldsymbol{t}=-\boldsymbol{r}. \tag{4.33}$$

(e) Expand $\boldsymbol{V}$ by applying Modified Gram-Schmidt method

$$\boldsymbol{V}=\mathrm{ModGS}(\boldsymbol{V}|\boldsymbol{t}).$$

The approach by adopting the Jacobi-Davidson method to solve the flutter eigenproblem could be categorized as a $k-$method in flutter analysis[Hodges and Pierce, 2011].

Eigenvalue selection criterion

The Jacobi-Davidson method converges to eigenvalues that are within a selected spectrum of the eigenproblem. The number of eigenvalues in this spectrum is at most the size of the search space and is therefore limited by computational cost. For this reason, it is imperative to locate the spectrum that is the most important to evaluate the flutter constraint. Therefore, an eigenvalue selection criterion which can narrow this spectrum to the most critical eigenvalues for flutter is used.

In aeroelastic analysis, a positive real part of an eigenvalue results in flutter. Therefore, finding the eigenvalue with the largest real part is essential to evaluating the flutter constraint. Vibration frequency is the physical meaning of the imaginary part of each eigenvalue. Lower frequencies of vibration tend to be flutter-critical since higher frequency vibrations tend to be attenuated by aerodynamic damping. Therefore, eigenvalues which have the largest real part as well as a relatively small absolute value of the imaginary part, are desired.

The criterion adopt in this research has the following expression,

$$\hat{\lambda}=\underset{\lambda}{\mathrm{Max}}\left(\Re(\lambda)-\alpha\Im(\lambda)\right). \tag{4.34}$$

$\theta$are eigenvalues, $\hat{\theta}$ is the fitness of each eigenvalue and in order to determine the flutter constraint, the eigenvalue with the largest fitness is sought, α is a weight constant which can adjust frequency filtering. The contour of this criterion is shown below, see Figure 4.20

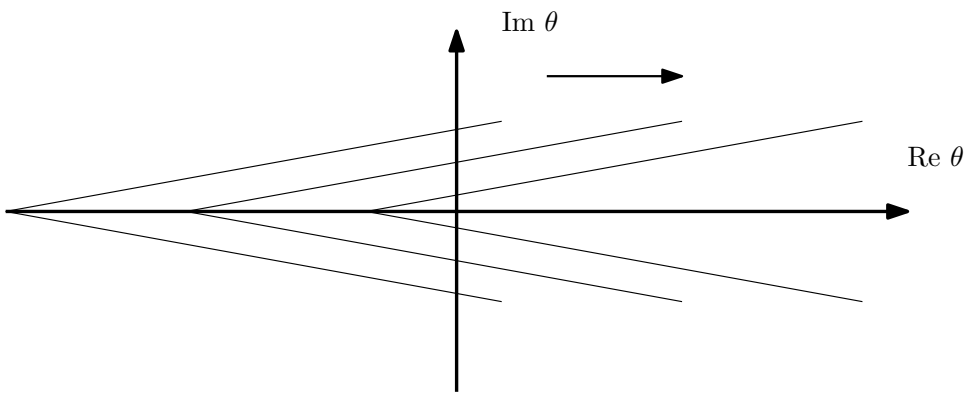

Figure 4.20: The contour of eigenvalue selection criterion

Derivative computation

The gradient of eigenvalue λ with respect to the design variables is required for design optimization. This gradient is obtained by adopting the following approach. By solving the eigenproblem, the left eigenvector $\boldsymbol{v}$ can be obtained by solving the conjugate eigenproblem of Eq. 3.15, which is

$$\left((\lambda^H)^2 \boldsymbol{J}_2^H + \lambda^H \boldsymbol{J}_1^H + \boldsymbol{J}_0^H\right) \boldsymbol{v} = \boldsymbol{0}. \tag{4.35}$$

And the left eigenvector satisfy following expression,

$$\boldsymbol{v}^H \left(\lambda^2 \boldsymbol{J}_2 + \lambda \boldsymbol{J}_1 + \boldsymbol{J}_0\right) = \boldsymbol{0}. \tag{4.36}$$

Assume x_i is the ith design variable. Now we can compute the derivative of Eq. 3.15, shown below,

$$\begin{aligned} 0 = &\frac{\partial \boldsymbol{J}_0}{\partial x_i}\boldsymbol{u} + \boldsymbol{J}_0\frac{\partial \boldsymbol{u}}{\partial x_i} + \lambda\frac{\partial \boldsymbol{J}_1}{\partial x_i}\boldsymbol{u} + \lambda\boldsymbol{J}_1\frac{\partial \boldsymbol{u}}{\partial x_i} + \frac{\partial \lambda}{\partial x_i}\boldsymbol{J}_1\boldsymbol{u} \\ &\lambda^2\frac{\partial \boldsymbol{J}_2}{\partial x_i}\boldsymbol{u} + \lambda^2\boldsymbol{J}_2\frac{\partial \boldsymbol{u}}{\partial x_i} + 2\lambda\frac{\partial \lambda}{\partial x_i}\boldsymbol{J}_2\boldsymbol{u}. \end{aligned} \tag{4.37}$$

left multiplying the left eigenvector with Eq. 4.37 yield,

$$\begin{aligned} 0 = &\boldsymbol{v}\frac{\partial \boldsymbol{J}_0}{\partial x_i}\boldsymbol{u} + \lambda\boldsymbol{v}^H\frac{\partial \boldsymbol{J}_1}{\partial x_i}\boldsymbol{u} + \lambda^2\boldsymbol{v}^H\frac{\partial \boldsymbol{J}_2}{\partial x_i}\boldsymbol{u} \\ &\boldsymbol{v}^H\left(\lambda^2\boldsymbol{J}_2 + \lambda\boldsymbol{J}_1 + \boldsymbol{J}_0\right)\frac{\partial \boldsymbol{u}}{\partial x_i} + \frac{\partial \lambda}{\partial x_i}\left(\boldsymbol{v}^H\boldsymbol{J}_1\boldsymbol{u} + 2\lambda\boldsymbol{v}^H\boldsymbol{J}_2\boldsymbol{u}\right), \end{aligned} \tag{4.38}$$

considering Eq. 4.36, the Eq. 4.38 can be simplified as

$$\frac{\partial \lambda}{\partial x_i} = -\frac{\boldsymbol{v}^H \left(\lambda^2 \frac{\partial \boldsymbol{J}_2}{\partial x_i} + \lambda \frac{\partial \boldsymbol{J}_1}{\partial x_i} + \frac{\partial \boldsymbol{J}_0}{\partial x_i} \right) \boldsymbol{u}}{\beta + 2\lambda\gamma}. \tag{4.39}$$

where

$$\beta = \boldsymbol{v}^H \boldsymbol{J}_1 \boldsymbol{u}$$

$$\gamma = \boldsymbol{v}^H \boldsymbol{J}_2 \boldsymbol{u}.$$

Eq. 4.39 can be used to evaluate the gradient of the eigenvalue. In this particular research, the $\boldsymbol{J}_1$ is not a function of design variable thus we have

$$\lambda \boldsymbol{v}^H \frac{\partial \boldsymbol{J}_1}{\partial x_i} \boldsymbol{u} = 0. \tag{4.40}$$

So the Eq. 4.39 can be further simplified as

$$\frac{\partial \lambda}{\partial x_i} = -\frac{\boldsymbol{v}^H \left(\lambda^2 \frac{\partial \boldsymbol{J}_2}{\partial x_i} + \frac{\partial \boldsymbol{J}_0}{\partial x_i} \right) \boldsymbol{u}}{\beta + 2\lambda\gamma}. \tag{4.41}$$

By applying the method described above, the gradient of the eigenvalue picked can be computed. However, the Jacobi-Davidson method combined with the eigenvalue selection criterion does not trace a single eigenvalue. Instead the proposed method finds the eigenvalue with largest fitness value. As a result the gradient calculated by this method may cause the optimization algorithm to fail in some situation, as seen in Figure4.21

As shown in this figure, the eigenvalue with the greatest fitness change from λ_1 to λ_2 with the increase of the design variables. If the gradient of the eigenvalue at design point A is calculated, the method described in this section would compute the gradient of λ_1. But the true gradient needed for optimization is the gradient of λ_2. The difficulty can be solved by utilizing the Finite Difference Method to compute the gradient, though the computational cost of the much higher.

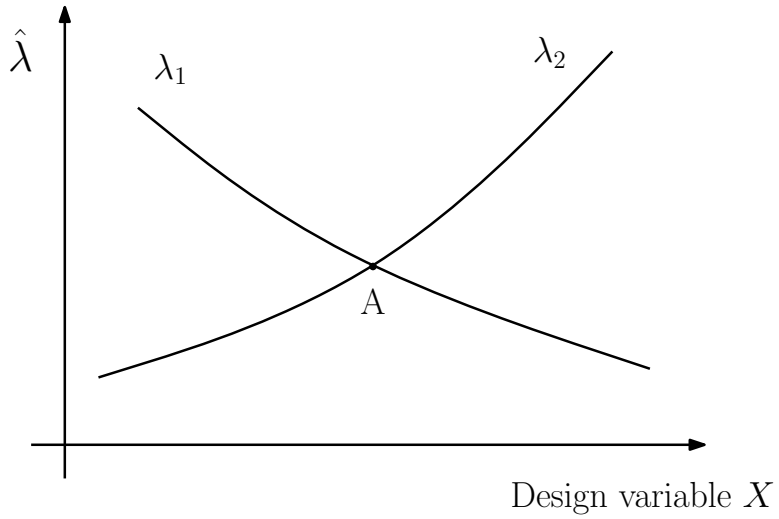

Figure 4.21: Gradient failed situation

4.5 The stress constraint

4.5.1 Aerodynamic solver

TriPan is used as the aerodynamic solver. TriPan is a three-dimensional panel method for the solution of the Prandtl-Glauert equations. It uses constant source and doublet singularity elements distributed over a watertight surface mesh. Forces, moments as well as lift, drag and moment coefficient can be evaluated. A key feature of TriPan is its discrete adjoint implementation which enables the efficient evaluation of the gradient of aerodynamic functions of interest with respect to both geometric and aerodynamic design variables.

4.5.2 Structural solver

The structural analysis is performed using Toolkit for the Analysis of Composite Structures (TACS), a parallel finite-element code designed specifically for the design optimization of stiffened, thin-walled composite structures using either linear or geometrically nonlinear developed by Kennedy and Martins [Kennedy and Martins, 2014].

4.6 The Optimizer

The HOpt is a python-based optimizer for parallel large-scale gradient-based optimization with optional Hessian-vector product capabilities. HOpt uses an interior-point method with various barrier updating schemes including a Fiacco and McCormick and a Mehro-

tra predictor-corrector scheme. A limited-memory BFGS updating method is used to form an approximate Hessian, and its inverse.

CHAPTER 5

RESULT

In this chapter, the results computed by the optimization approach introduced in previous chapters are presented. Three factors in optimization design are studied in this research. First the effect of the flutter constraint is examined. In order to investigate how the flutter constraint will affect the structural optimization, two cases are conducted here. Utilizing the optimization process to FEM model built previously, only apply the stress constraint at first, then the flutter constraint is added to determine the effect of the flutter constraint. By comparing these two cases, whether the structure design is influenced by flutter constraint can be known.

Apart from design variables already included in the optimization process, there are other system parameters which can make an impact on the optimized result. The effects of two system parameters are investigated in this research. One this the aspect ratio. The aspect ratio can greatly affect the structure stiffness of the wing as well as the aerodynamic loading. By setting the aspect ratio to three different values, how will this parameter affect the optimum structure mass and component thickness distribution can be determined.

The other parameter's effect studied is the quantity of propellers. Different configurations of propellers would change the flow field over the wing surface thus affecting the distribution of the aerodynamic loading. By change the number of propellers mounted on the wing,effect of this parameter on the optimization result can be determined.

Since the FEM model just contains the semi-wing structure and set clamped boundary condition at the wing root symmetric plane, all the wing structural mass mentioned below is just the mass of the semi-wing. The mass of the propellers and mass of the motors are not included. In this research, the relative objective function change is used as the optimization converge criterion. The relative objective function value change tolerance is set to 10^{-4} in most cases. The lower bound of design variables is set to 0.1mm due to consideration of reality.

5.1 Effect of flutter constraint

In this section, the effect of the flutter constraint on the optimized wing structure is examined. First, minimum mass designs, subject only to stress constraints, are obtained. Next, the flutter constraint is added and the difference between the two sets of wing designs is examined.

The optimization condition is set to level cruise stage of the LEAPTech airplane. The structure model constructed in last chapter is used. On the condition of adopting relative objective function change as converging criterion, the algorithm can converge in less than 100 iterations, as seen in Figure 5.1. However, the optimization process would take more steps to meet the converge criterion than the case when stress is the only constraint.

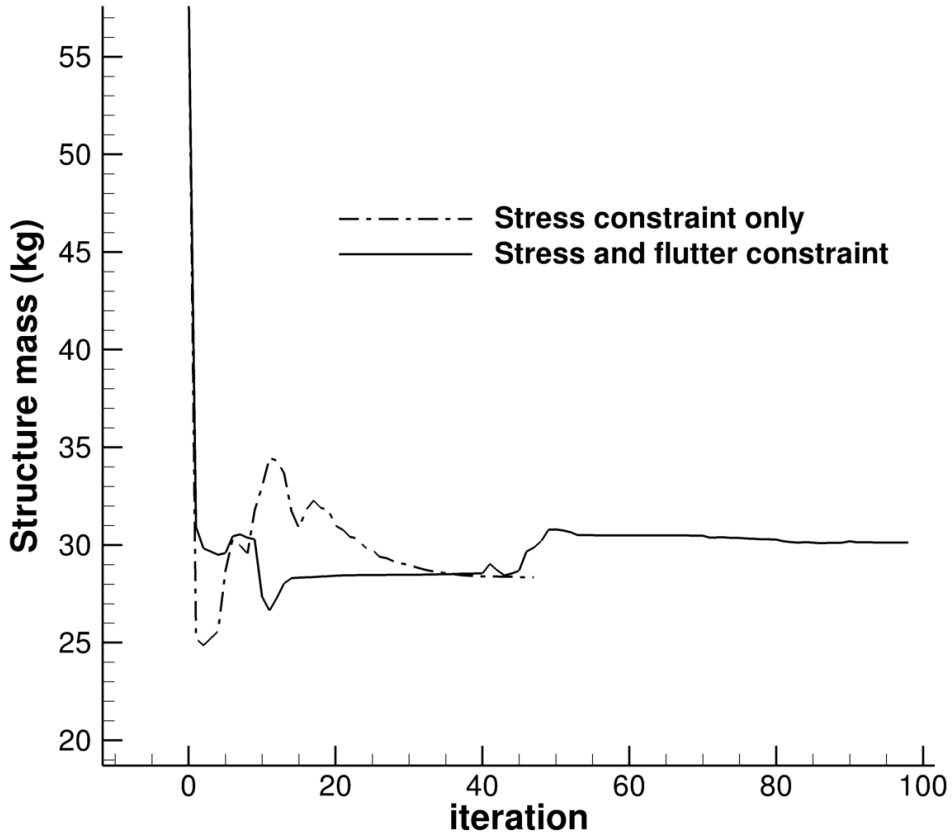

Figure 5.1: Algorithm converge curve with and without flutter constraint

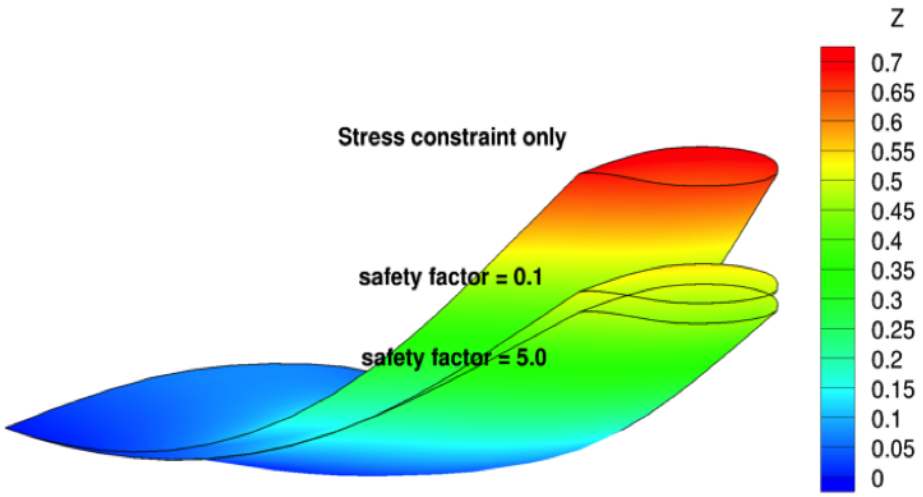

Figure 5.2: Displacement under different optimization case

The result of the optimization is listed in Table. 5.1. The displacement of each optimization case is shown in Figure 5.2. According to this figure, flutter constraint will lower the tip displacement. And the larger the flutter safety factor, the smaller displacement. As seen from the table, the optimum structure mass increase when the flutter constraint is added. This means the flutter constraint limits the structure. By changing the safety factor from 0.1 to 5.0, the optimum mass also increases. Two conclusions can be drawn here:

1. The flutter constraint increases the optimum mass
2. The flutter constraint with a larger safety factor leads to a stricter requirement and a wing design with a higher mass

Table 5.1: Effect of the flutter constraint

	Stress constraint only	safety factor = 0.1	safety factor = 5.0
Structure mass (kg)	28.35	30.11	32.42
critical eigenvalue real part		-0.27	-5.47
KS value	0.9949	0.9936	0.9926
Trim constraint	1.0033	1.0035	1.0039

Here that the stress constraint is described by the Kreisselmeier-Steinhauser (KS) function which is widely used constraint aggregation method for gradient optimization [Martins and Poon, 2005]. A KS function value equals to one means some of the elements in the structure model reach maximum allowable stress. The Trim constraint value is then calculated

by following equation,

$$\text{Trim constraint value} = \frac{L}{Wn},$$

where L is the total aerodynamic left, W is the aircraft weight, and n is the vertical load factor.

But there are some noted limitations here. Since the gradient of the eigenvalue computation may failed at a particular case, the structure critical damping is not very close to the boundary when compare with the stress and trim constraint. This may cause the optimum structure mass to be more conservative than real value. Applying the Finite Difference Method (FDM) or stricter converge criterion may solve this problem.

5.2 Effect of aspect ratio

In this section, optimization results with stress constraints are shown. There are three wing structures with different aspect ratio that are optimized. The selected wing aspect ratios are 15, 17.4 and 20. The lowest structure mass for each aspect ratio was obtained. The results of these optimizations with different aspect ratio are listed in the Table 5.2. According to the result, the increase rate of the structure mass is not linear with the increase rate of aspect ratio. Since the wing is scaled in the spanwise direction to achieve different aspect ratio, the mass should be a linear function of the aspect ratio if there were no stress or flutter constraints. However, the DEP aircraft wing, increasing aspect ratio brings an increase in the mass greater than the linear relation. This is due to the fact that the higher aspect ratio wings are more susceptible to flutter instability and have higher stresses.

Table 5.2: Effect of the aspect ratio

Aspect ratio	15	17.4	20
Structure mass (kg)	24.23	30.11	37.76
Mass increase ratio	0%	24.27%	58.24%
Span increase ratio	0%	16.00%	33.33%

The Figure 5.3 shows the components thickness and stress distribution. Compare to the lower aspect ratio wing, the higher aspect ratio wing has a thicker wing tip area component. This shows that the stress and flutter problem possible easily happened at a locate far from the wing root, as depicted in Figure 5.5. The Figure5.4 show the component stress

distribution all over the wing. The stress distribution shows that the higher aspect ratio structure suffer from severer stress problem. The local stress level is higher when compare with short wings.

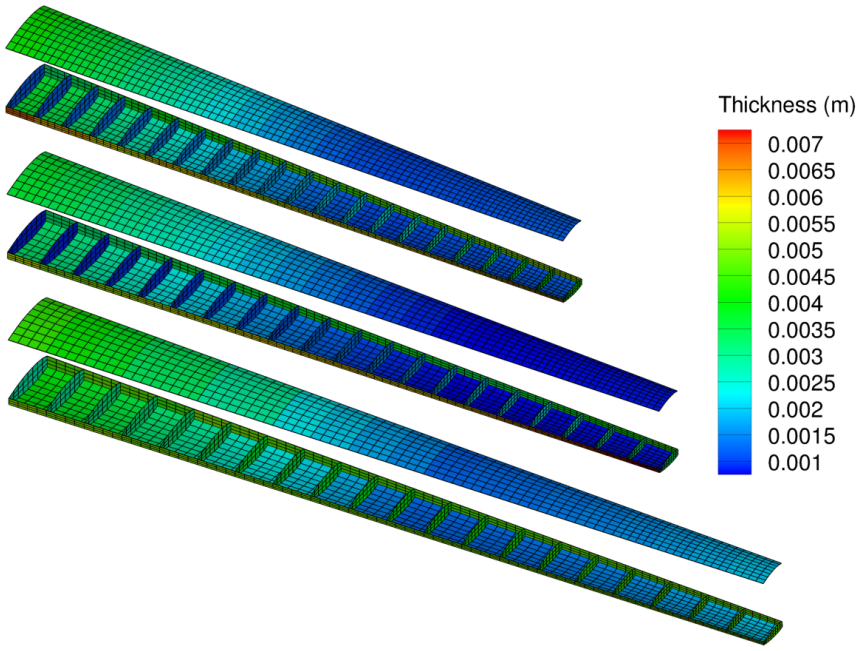

Figure 5.3: Optimum thickness of the structure

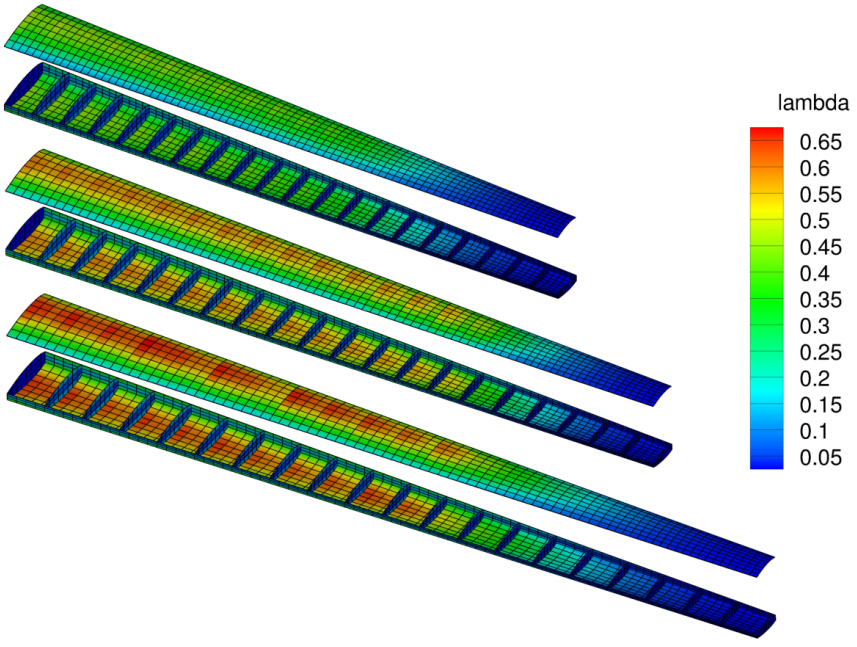

Figure 5.4: Stress distribution of the optimum structure

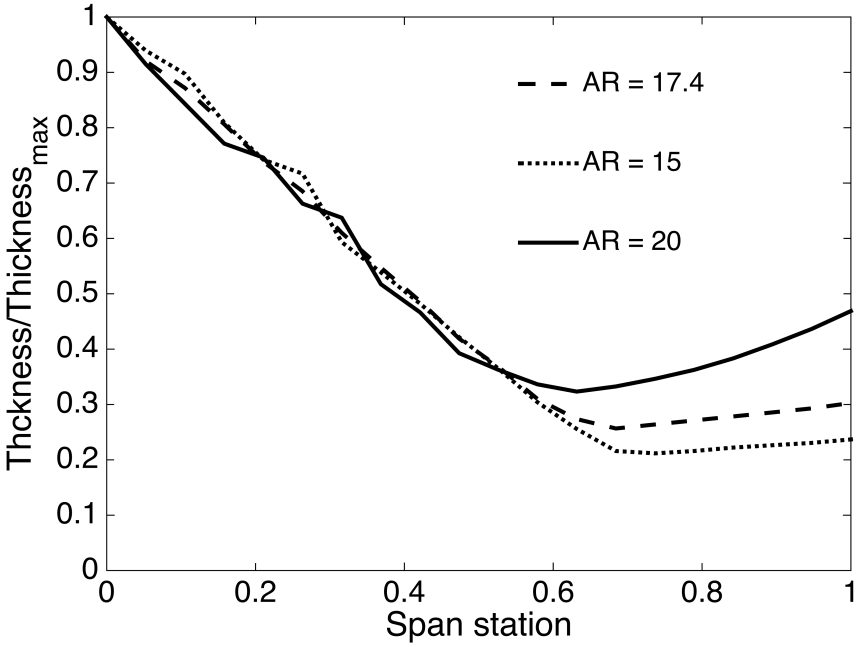

Figure 5.5: Thickness distribution of wings with different aspect ratio

5.3 Effect of propeller quantity

In this section, the effect of number of propellers on DEP aircraft wing structure design is discussed. The high aerodynamic efficiency, for instance, the high $C_{L_{max}}$ can reach 5, comes from its unique way to distribute propellers along the wing span direction. In order to investigate the effect of the number of propellers, three DEP configurations with different number of propellers were chosen. Although the quantities are different, the propellers are still need to meet the thrust requirement. Figure5.6 and Figure5.7 shows the upwash velocity and pressure coefficient distribution of a wing with a five- and a three-propeller configuration.

The result is in Table. 5.3. From the data, it can be concluded that although more propellers distributed on the leading edge of the wing can improve the aerodynamic efficiency, but higher aerodynamic loading can easily cause the structure easier suffer from flutter instability or stress failure. This may be caused by propellers distributed span wise increase aerodynamic loading. For this reason, the more propellers, the larger aerodynamic loading the structure will suffer, thus the higher possibility to have flutter instability or larger local stress.

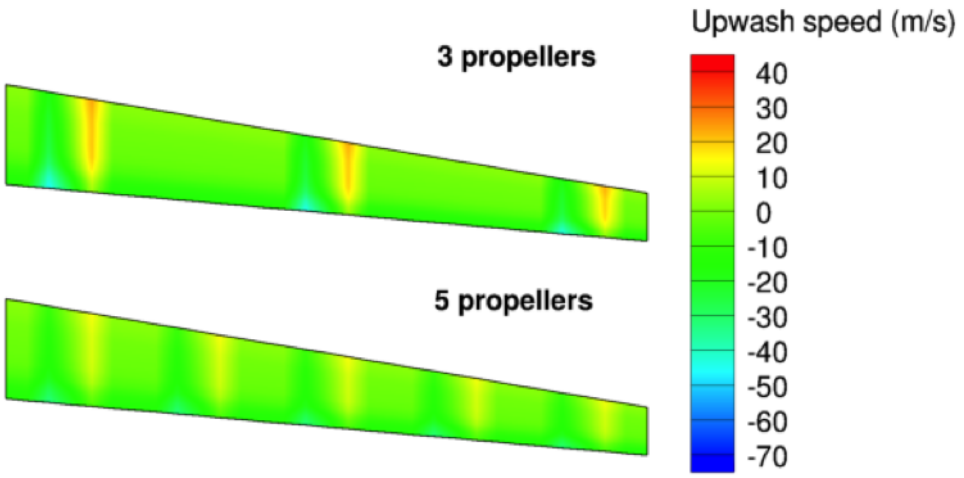

Figure 5.6: Upwash velocity distribution of wing with 3 and 5 propellers

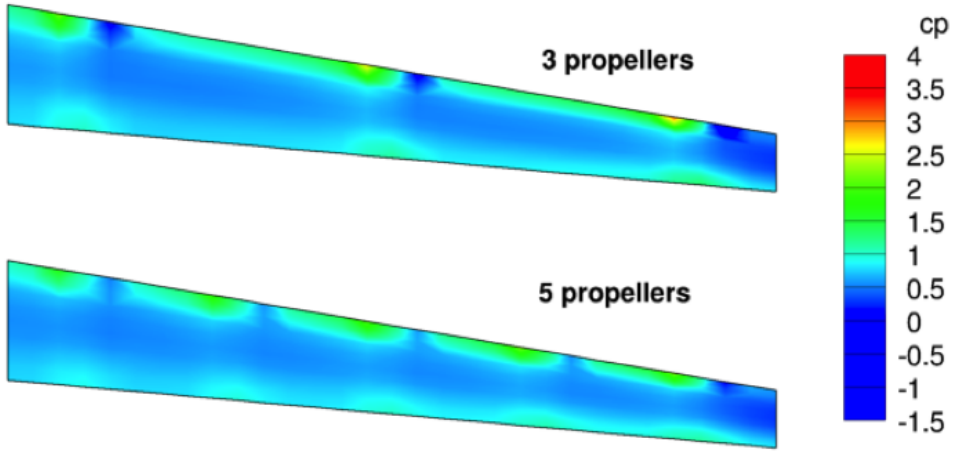

Figure 5.7: Pressure coefficient distribution of wing with 3 and 5 propellers

Table 5.3: Effect of the propeller quantity

Number of propellers	3	5	10
Structure mass (kg)	26.26	26.65	30.11
Mass increase ratio	0%	0.01%	14.66%

5.4 Effect of follower force

By coupling follower force into optimization with stress constraint alone, how will it affect optimum design can be investigated. Four different cases were set up with no follower force, one times thrust, two times thrust and four times thrust to follower force. Optimization result and displacement situations shown below,

Table 5.4: Effect of the follower force

Follower force	0	1 time thrust	2 times thrust	4 times thrust
Structure mass (kg)	22.491	21.943	20.258	18.908
Mass increase ratio	0%	−2.44%	−9.93%	−15.93

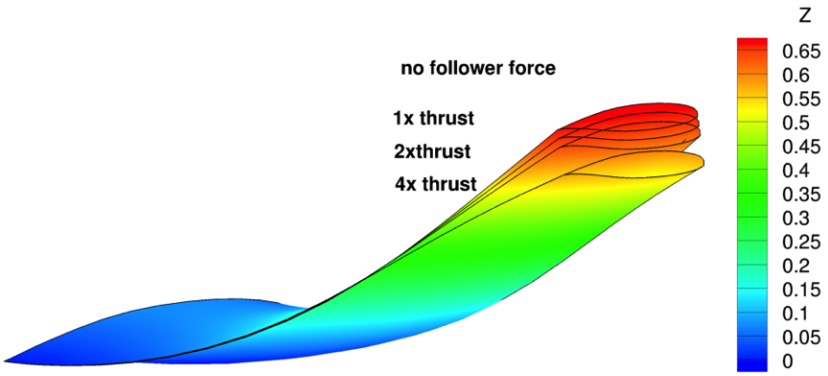

Figure 5.8: Displacement under different follower force

The table above shows that the follower force from the propeller tractive force can alleviate stress of the wing and result to lighter optimum structure. The figure shows that the follower force could reduce displacement. In order to explain the mechanism, a "negative wing bending-twist coupling" could be defined, which means when the wing has a bend upward, its section will also have a negative twist because of deformation, and vice versa. On this condition, the direction of the follower force is opposite with the deformation thus will thus reduce displacement and alleviate the stress level. This can be prove by the figure below, see Figure 5.9,

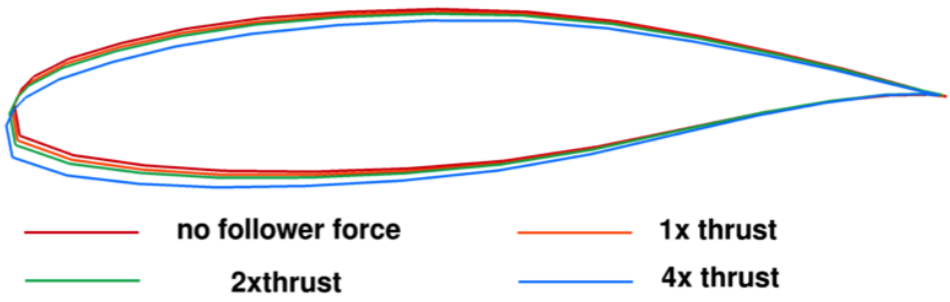

Figure 5.9: Deformation of the wing tip section

From this figure it can be observed that all the wing tip sections have negative twist

because of deformation.

5.5 Conclusion

Based on these results, the following claims can be made about the DEP aircraft optimization:

1. Based on the DEP aircraft wing structure optimization, stress constraints are not the only constraint that would impact the design. Furthermore, stress constraints alone will not be sufficient to ensure flight safety. Flutter may still cause structural failure even if the strength constraints are satisfied. The flutter constraint introduced in this research reduces this possibility.

2. The aspect ratio and quantity of distributed propellers are important system parameters in the structural design and may affect the optimization result. Larger aspect ratio or more propellers can lead to a more flexible structure or larger aerodynamic loading. Both of these make the wing structure more vulnerable to stress failure and flutter instability. In order to guarantee that the wing is free from possible failure, it is important to locate the balance between high aerodynamic efficiency and structure strength as well as flutter stability.

CHAPTER 6

FUTURE WORK

Apart from the tools and techniques developed and applied in this research, here are some further attempts which have the potential to improve the reality, credibility, and accuracy of the optimization result.

- In order to express the aerostructure in an accurate and realistic manner, nonlinearity should be take into consideration when the aspect ratio is large. The wing structure is flexible and can have large deformation under certain loading. Possible nonlinear phenomena including geometric nonlinearity, aerodynamic nonlinearity and dynamic nonlinearity.

- Discussed in previous chapter, present method to obtain gradient of eigenvalue with respect to design variables in the Jacobi-Davidson method will be not accurate when the critical eigenvalue changes. Although utilizing the Finite Difference method (FDM) can capture the switch of critical eigenvalue and return the correct gradient, high computational cost makes it hard to apply in practical approaches. Better option is to combine present analytical gradient calculation computation method with FDM. In this better approach, algorithm may be able to recognize when the critical eigenvalue switches happen and apply FEM instead of analytical way which used any other situation.

- The interaction between propellers and wing should be considered in a more sophisticated way. Not only the affect of propellers on wing, but also how the wing influence the propellers flow field can be consider to receive a more realistic and accurate aerodynamic loading estimation. Currently, the Computational Fluid Dynamics (CFD) is widely used in both academics and industry domain to solve complicated aerodynamic problems. Coupling CFD with present approach has high potential to conduct better aerodynamic analysis of the DEP aircraft. However, long computational time of

CFD should also be noticed before we apply this optimization approach in the aircraft preliminary design stage.

- Apart from the follower force and mass inertia, motor and propeller gyroscopic moment and shaft moment can affect structure dynamic characteristic, especially when the wing is very flexible and may have large displacement and deformation. Modeling motors and propellers with consideration of higher order effect can help to predict a more reliable optimization result. Also, the shaft moment should be considered in stress analysis.

- The Tripan is used to estimate aerodynamic loading for the TACS to evaluate the stress constraint. But since this way to generate aerodynamic force has not been coupled with propellers' effect. In the future, either the coupling between wing and propeller should be also considered in the Tripan, or other aerodynamic analysis method or tools should be used.

- In order to study follower force's effect thoroughly, it is necessary to coupling it with flutter constraint.

Bibliography

E. Albano and W. P. Rodden. A doublet-lattice method for calculating lift distributions on oscillating surfaces in subsonic flows. *AIAA Journal*, 7(2):279–285, 1969. ISSN 0001-1452.

M. S. Alex, B. JoeBen, D. M. Mark, J. F. William, and K. B. Nicholas. Drag reduction through distributed electric propulsion. 2014. doi:10.2514/6.2014-2851.

G. Ameyugo, M. Taylor, and R. Singh. Distributed propulsion feasibility studies. In *25th International Congress of the Aeronautical Sciences*, page 06, 2006.

J. D. Anderson. *Aircraft performance and design / John D. Anderson, Jr.* Boston : WCB/McGraw-Hill, c1999., 1999. ISBN 0070019711.

K. Y. Billah and R. H. Scanlan. Resonance, tacoma narrows bridge failure, and undergraduate physics textbooks. *American Journal of Physics*, 59(2):118–124, 1991.

R. Bisplinghoff, H. Ashley, and R. Halfman. *Aeroelasticity*. Dover Books on Aeronautical Engineering Series. Dover Publications, 1996. ISBN 9780486691893.

M. Blair. A compilation of the mathematics leading to the doublet lattice method, 1992.

C. E. Cesnik and W. Su. Nonlinear aeroelastic simulation of x-hale: a very flexible uav. In *49th AIAA Aerospace Sciences Meeting including the New Horizons Forum and Aerospace Exposition, Orlando, Florida*, 2011.

C. E. Cesnik, P. J. Senatore, W. Su, E. M. Atkins, C. M. Shearer, and N. A. Pitcher. X-hale: a very flexible uav for nonlinear aeroelastic tests. *Paper No. AIAA-2010-2715, Proceedings of*, 2010.

J. Conway. Analytical solutions for the actuator disk with variable radial distribution of load. *Journal of Fluid Mechanics*, 297:327 – 355, 1995.

F. Eastep and S. McIntosh. Design of minimum-mass structures with specified stiffness properties. *AIAA Journal*, 6(5):962–964, 1968.

A. S. Gohardani, G. Doulgeris, and R. Singh. Challenges of future aircraft propulsion: A review of distributed propulsion technology and its potential application for the all electric commercial aircraft. *Progress in Aerospace Sciences*, 47(5):369 – 391, 2011. ISSN 0376-0421.

I. S. Gradshteyn, I. M. Ryzhik, and A. Jeffrey. *Table of integrals, series, and products*. San Diego : Academic Press, c2000., 2000. ISBN 0122947576.

R. L. Harder and R. N. Desmarais. Interpolation using surface splines. *Journal of Aircraft*, 9(2):189–191, 1972. ISSN 0021-8669.

D. H. Hodges and G. A. Pierce. *Introduction to structural dynamics and aeroelasticity*. Cambridge aerospace series: 15. New York : Cambridge University Press, 2011., 2011. ISBN 9781139127882.

D. H. Hodges, M. J. Patil, and S. Chae. Effect of thrust on bending-torsion flutter of wings. *Journal of aircraft*, 39(2):371–376, 2002.

B. J. Holmes. Flight evaluation of an advanced technology light twin-engine airplane (atlit). 1977.

R. Jaiman, P. Geubelle, E. Loth, and X. Jiao. Transient fluid–structure interaction with non-matching spatial and temporal discretizations. *Computers & Fluids*, 50(1):120–135, 2011.

R. M. Jones. *Mechanics of composite materials*. CRC Press, 1998.

G. J. Kennedy and J. R. Martins. A parallel finite-element framework for large-scale gradient-based design optimization of high-performance structures. *Finite Elements in Analysis and Design*, 87(0):56 – 73, 2014. ISSN 0168-874X.

G. J. Kennedy, G. K. Kenway, and J. R. Martins. Towards gradient-based design optimization of flexible transport aircraft with flutter constraints. In *Proceedings of the 15th AIAA/ISSMO Multidisciplinary Analysiand Optimization Conference*, 2014.

H. D. Kim and J. D. Saunders. Embedded wing propulsion conceptual study. Technical report, 2003.

A. Ko, J. A. Schetz, and W. H. Mason. International symposium on air g engines. pages 71 – 72, 2003.

C. D. Kolbe and F. W. Boltz. *The forces and pressure distribution at subsonic speeds on a plane wing having 45 of sweepback, an aspect ratio of 3, and a taper ratio of 0.5.* NACA, Washington, 1951.

L. Leifsson, A. Ko, W. Mason, J. Schetz, B. Grossman, and R. Haftka. Multidisciplinary design optimization of blended-wing-body transport aircraft with distributed propulsion. *Aerospace Science and Technology*, 25(1):16 – 28, 2013. ISSN 1270-9638.

J. Martins and N. M. Poon. On structural optimization using constraint aggregation. In *VI World Congress on Structural and Multidisciplinary Optimization WCSMO6, Rio de Janeiro, Brasil*, 2005.

D. M. Pargett and M. D. Ardema. Flight path optimization at constant altitude. *Journal of guidance, control, and dynamics*, 30(4):1197–1201, 2007.

M. Patterson, M. Daskilewicz, and B. German. Conceptual design of electric aircraft with distributed propellers: Multidisciplinary analysis needs and aerodynamic modeling development. 2013.

M. D. Patterson and B. German. Wing aerodynamic analysis incorporating one-way interaction with distributed propellers (aiaa 2014-2852). 2:1614 – 1626, 2014.

D. P. Raymer. *Aircraft design : a conceptual approach / Daniel P. Raymer.* AIAA education series. Reston, Va. : American Institute of Aeronautics and Astronautics, c2006., 2006. ISBN 1563478293.

W. Rodden and E. Johnson. *MSC/NASTRAN aeroelastic analysis user's guide.* MSC, 1994.

Y. Saad. *Numerical methods for large eigenvalue problems*, volume 158. SIAM, 1992.

Y. Saad and M. H. Schultz. Gmres: A generalized minimal residual algorithm for solving nonsymmetric linear systems. *SIAM Journal on scientific and statistical computing*, 7(3): 856–869, 1986.

E. Simodynes. Gradient optimization of structural weight for specified flutter speed. *Journal of Aircraft*, 11(3):143–147, 1974.

G. L. Sleijpen and H. A. Van der Vorst. A jacobi–davidson iteration method for linear eigenvalue problems. *SIAM Review*, 42(2):267–293, 2000.

G. L. Sleijpen, A. G. Booten, D. R. Fokkema, and H. A. Van der Vorst. Jacobi-davidson type methods for generalized eigenproblems and polynomial eigenproblems. *BIT Numerical Mathematics*, 36(3):595–633, 1996. ISSN 0006-3835.

M. J. Smith, D. H. Hodges, and C. E. S. Cesnik. Evaluation of computational algorithms suitable for fluid-structure interactions. *Journal of Aircraft*, 37(2):282–294, 2000. ISSN 0021-8669.

F. Stern, H.-T. Kim, V. C. Patel, and H.-C. Chen. Computation of viscous flow around propeller-shaft configurations. Technical report, Iowa Institute of Hydraulic Research, the University of Iowa, 1986.

D. Strash, J. Nathman, B. Maskew, and F. Dvorak. The application of a low-order panel method-program vsaero to powerplant and airframe flow studies. 1984.

D. Tang and E. Dowell. Effects of geometric structural nonlinearity on flutter and limit cycle oscillations of high-aspect-ratio wings. *Journal of Fluids and Structures*, 19(3):291 – 306, 2004. ISSN 0889-9746.

J. Walsh, W. Stroud, R. Weston, H. Dunn, and J. Barthelemy. Minimum weight structural design of three alternate hsct concepts, 2002.